Argelander-
Institut
für
Astronomie

UNIVERSITÄT BONN

Rheinische
Friedrich-Wilhelms-
Universität Bonn

Diagnostic of the conditions at the base of the optically thick winds of Wolf-Rayet stars in the Galaxy and the LMC

Vsevolod Nedora

Masterarbeit in Astrophysik
angefertigt im Argelander-Institut für Astronomie

vorgelegt der
Mathematisch-Naturwissenschaftlichen Fakultät
der
Rheinischen Friedrich-Wilhelms-Universität Bonn

September 2018

I hereby declare that this thesis was formulated by myself and that no sources or tools other than those cited were used.

Bonn, ...
Date Signature

1. Gutachter: Prof. Dr. Norbert Langer
2. Gutachter: PD. Dr. Jürgen Kerp

Abstract

Wolf-Rayet stars are luminous stars in the late stage of evolution, showing high mass-loss rates and having optically thick stellar winds. The mass-loss rate is of high importance for stellar evolution and, in case of massive post-main sequence stars, strongly affects the star's spectroscopic appearance.
In the Wolf-Rayet phase, optically thick winds make deeper layers and the mechanism of wind acceleration unobservable. That might contribute to the disagreement between the stellar structure calculations and observations.
Here we study the sonic point conditions of the H-free Wolf-Rayet stars of nitrogen sequence (WNE) in the Galaxy and the Large Magellanic Cloud, complimenting it by the analysis of the uncertainties of the observed physical parameters and the evolutionary stage of these stars. For this we compute 1D hydrodynamic stellar structure models of massive helium stars with different metallicities defining the outer boundary at the sonic point.
We confirm that the models corresponding to the Galactic WNE stars, have their outflow launched to supersonic velocities by the radiative force from the iron opacity bump at a temperature of the order of 200kK. Models that correspond to the LMC WNE stars show that only the most luminous stars have such mechanism, while most of the WNE population have their winds accelerated by the radiative force from the helium-II opacity bump and have a sonic point temperature of order 60kK. However, for a given star, the wind launching mechanism depends on metallicity.
For the Galactic WNE stars, withing the considered uncertainties the temperature at the sonic point mostly depend on stellar luminosity, in case of adopting the luminosities from Hamann et al. (2006) as well as from GAIA DR2 (Brown et al. 2018). However, the relation becomes less tight in the second case. Similarly, there appears to be a relation between the sonic point and the photospheric temperatures in the first case, however, it becomes much less apparent if the GAIA luminosities are used (the photospheric conditions and mass-loss rate were not modified for new luminosities).
For the WNE stars in the LMC, there are two, compact and extended domains of subsonic structures. Within both, the physical parameters at the sonic point mostly depend on stellar luminosity. We find no clear relation between the sonic point and photospheric properties of these stars.

Acknowledgements

I would like to thank, first of all, my supervisor Professor Norbert Langer. His advise, patience, encouragement and his trust in me have been invaluable. His teaching goes far beyond the academic disciplines, that I have no doubt benefited from. Professor Langer gave me a priceless experience of working in a competitive academic environment, where the expectations are high and the time management is of essence.
An equal of value experience I gained from working with Doctor Luca Grassitelli, who has supervised my work as well. The amount and the depth of knowledge I acquired, is a direct result of all the time and effort he has devoted to my thesis. Our mutual strive for the quality and robustness of the research had provided me with a standard of work I shall strive for in my academic career. The freedom and the considerable degree of independence had allowed me not only to preserve the deep interest in research, but also to conduct my own investigations and then defend the results against professional criticism. For this, and for countless other lessons, I am forever grateful to Dr. Grassitelli.
In addition I would like to thank all the friends I have maid during my study at AIfA. Marcus Keil, Beatriz Hernandez Martin, Davit Alkhanishvili, Katharina Hortmanns, without your support, mental and professional, my thesis as it is now would have never seen the light of the day.
But there are people, without whom, I would have never even considered studying science left alone to embark on the challenge of doing it in Germany. My Father and Mother, Sergey and Anna Nedora, I bow deeply in gratitude. Everything I was, I am and I will ever be, I owe it to you, and all the words of all the languages are not enough for me to express how much I value it and how thankful I am.
Finally, I would like to thank the Argelander Institut für Astronomie, and everyone who works there, for their support and help, the Bonn-Cologne Graduate School of Physics and Astronomy for investing their time in me and supporting me.

Contents

Chapter 1.

Introduction

The aim of this work is to investigate the physical conditions in outer layers of massive post-main sequence stars, focusing on the outflowing material, the stellar wind, and on effects it has on the observed properties of these stars.
The thesis is structured as follows. In the first chapter we provide a brief overview on sections of stellar structure and evolution relevant for this work. In the second chapter, we explain the most important theoretical concepts that we base our work upon and discuss the numerical methods and techniques used. In the third chapter we present the results of our analysis of the WNE stars in the Galaxy. It follows by the fourth chapter, where we discuss the results of the study of WNE stars in the Large Magellanic Cloud. In the fifth chapter we summarize the main results of this work, draw the conclusion and provide a discussion.

1.1. Stars

In a highly simplified manner stars can be defined as self-gravitating spheres of hot plasma that produce energy via thermonuclear fusion in their interior. Energy produced by the fusion makes stars hot and so they shine for a prolong amount of time. The main physical processes governing the stellar life are the following. First, stars produce energy via complex chain of fusion reactions in their cores, or, if the conditions are met, in the surrounding areas. Second, this energy is transported outwards by two main physical processes: convection and radiation transport. Third, this energy is emitted at the surface in form of radiation and kinetic energy of the outflowing matter. The latter process is usually neglected, as for most stars during most of their lives the effect of mass loss is small. However, for massive stars in the late stages of evolution it is highly important.

Stellar Formation

Stars are born in giant clouds of cold molecular gas. Perturbed, for example by shock fronts from supernovae, a cloud fragments into regions of high density, or clumps. If the internal gas pressure is not strong enough to prevent the gravitational collapse of a clump, the Jeans instability[1] sets in and the fragment starts to collapse.
The shrinking of the radius of the collapsing clump implies that the gravitational energy decreases as well. Partially the energy is radiated away, while the rest goes to increase the internal energy, and in turn, the temperature of the collapsing matter. The density of the clump rises to the point where gas becomes optically thick, which prohibits further rapid cooling and the temperature starts to increase rapidly until the values of density and temperature becomes high enough for the deuterium to begin to fuse with hydrogen. This liberates enough energy to slow down the collapse

[1] If the mass of the clump: $M > M_J = (\pi/6) \cdot (c_s^3)/(G^{3/2}\rho^{1/2})$, where c_s is a local sound speed, ρ is the density.

and constitutes the emergence of a protostar. The continuous infill of matter from the surrounding cloud slows down as well. Having non-zero angular momentum, matter forms a circumstellar disk, and in certain cases, even stellar jets. The continuous increase in temperature and density proceeds until the hydrogen fusion sets in. The increased flux, and associated with it radiation pressure, pushes away the surrounding material, revealing the newly born main sequence star. This moment in stellar evolution is called Zero Age Main Sequence, or ZAMS.
The fragmentation of a molecular cloud into the collapsing clumps defines the mass distribution of future stars. In a highly simplified manner, all stars can be divided into three groups with regard to their mass: low mass stars $M \in (0.08, 2)M_{\odot}$, intermediate: $M \in (2, 8)M_{\odot}$ and massive stars $M > 8M_{\odot}$. The probability distribution function of a stars with certain masses to be born is called an initial mass function, (IMF) (Salpeter 1955). One of the important properties of IMF is that it predicts that massive stars are much less likely to be born. However, as it will be discussed later, these stars are of high importance for many brunches of astrophysics (Langer 2012).

1.2. Stellar Structure

1.2.1. Energy Source

There are two main energy sources for a star: gravitational contraction E_g and nuclear fusion E_{nuc}, where the former provides most of the energy in a short periods between nuclear burning stages.
During most of stellar life, the main energy source is thermonuclear fusion. It is an exothermic process, meaning that the production of heavy elements from light ones releases energy in form of radiation and kinetic energy of particles. The rate at which the energy is produced is set by how much energy is lost at the surface. The equilibrium associated with it is called thermal equilibrium. On a shorter timescale, a star strives to maintain a balance, called hydrostatic equilibrium. This is an equilibrium between an outward force, which is a pressure gradient, and the inward directed gravity force (Kippenhahn and Weigert 1990).

1.2.2. Energy Transport

Energy produced in the stellar interior is transported outwards via two main processes: radiation and convection.

Radiative energy transport

Radiative energy transport is the transport of energy mediated by the electromagnetic field which relies on the absorption or scattering of photons by the medium. In its nature, the radiative energy transport is a diffusive process. Thus, if the mean free math of the photon is small compare to the scale at which the thermodynamical quantities change, allows for the diffusive approximation to be used to describe the radiative transfer. This process depends on the properties of the media, and its opacity, which is the coefficient defining the attenuated intensity of radiation when it traverses a medium of a given density (Rybicki and Lightman 1979).
Traveling through the stellar interior via random walk, the photons undergo thermolisation, implying that the radiation spectrum becomes similar to the Plank spectrum (Rybicki and Lightman 1979, Kippenhahn and Weigert 1990).

Convection

In contrast to radiation, convection involves macroscopic bulk motion, driven by the buoyancy force. Thus convection violates local hydrostatic equilibrium. The basic mechanism of the

convection is the following. Let us consider a blob of plasma withing a star. Acquired an excess in energy, it expands which leads to the decrease in the relative density. Simultaneously subjected to buoyancy force, the blob starts to move upwards to regions with lower density, and therefore transporting energy. If the temperature and density stratification are such that the convective blob during its rise and expansion, keeps finding itself with a lower density compared to the surrounding medium, macroscopic motion of matter and energy taken place. This energy is then 'released' in cooler region implying a net transport of energy associated with such upward directed flow. Similarly, downward-directed flows are presents well in regions unstable to convection. In general, this movement is adiabatic, energy is not lost in the process, and such convection is called efficient. Convection is an inherently turbulent process, as the flow regime in convective zones is characterized by drastic changes in the macroscopic properties of the flow (Lighthill 1952).
The criterion to determine a layer in a star unstable to convection is (Kippenhahn and Weigert 1990):

$$L(r) > \frac{16\pi r^2 ac}{3\kappa\rho} T^3 \nabla T, \tag{1.1}$$

where $L(r)$ is the luminosity, r is the radius, T is the temperature and a is the radiation constant κ is the opacity, c is the speed of light, ρ is the density, a is the constant.
In the interior of massive stars, the large amount of energy locally produced satisfies the criterion and thus, the cores of massive stars are convective. High densities and low opacities ensures efficient energy transport.
In addition to being important for energy transport, convection also induces chemical mixing, transporting angular momentum, and oscillations (Kippenhahn and Weigert 1990).

Thermodynamical Equilibrium & Timescales

The longest timescale associated with the different phases of thermonuclear burning in a star is the **nuclear timescale**. This is defined by the total amount of fuel available multiplied by the fraction of the star, over which the fuel is burnt, and divided by the rate at which it is burnt:

$$\tau_{nuc} = \frac{\phi f_{nuc} M c^2}{L} \tag{1.2}$$

where f_{nuc} is the mass fraction of H burnt into He, ϕ is the fractional mass difference in the reaction (about 0.007 for H burning), L is the star's luminosity and c is the speed of light.
For a solar-like stars this timescale for hydrogen burning is of order of several billions of years.
The timescale time required for the gravitational potential energy of a star to be radiated is called Kelvin-Helmholtz time scale and is defined as

$$t_{KH} \approx \frac{GM^2/R}{L}. \tag{1.3}$$

This is the time that a star would need to contract if the nuclear burning in its interior stops, or the timescale necessary for a star not in thermal equilibrium to readjust. (Kippenhahn and Weigert 1990)
Dynamical time scale is an estimate on how long does it take for a star to expand or contract if the balance between pressure gradients and gravity is disrupted. It is the shortest timescale for a star.
Similarly, the microscopic collision timescales are of the same order. Thus the interior regions can quickly relax to local thermodynamic equilibrium (LTE). However, globally, the gradients of macroscopic physical quantities exist and, hence, a star is not globally in a thermodynamic equilibrium (Kippenhahn and Weigert 1990).
The set of equations that describes and governs the stellar structure is the following:

- conservation of mass,
- definition of velocity,
- conservation of momentum,
- energy transport equations,
- energy conservation equation.

Limit on radiative energy transport

The amount of energy that can be transported via radiation is not arbitrary high and is limited by the Eddington limit (Eddington 1925), which is achieved when the the inward directed force of gravity is balanced by the outward directed force created by the radiation pressure gradient alone. Assuming hydrostatic equilibrium:

$$\frac{d\upsilon}{dt} = -\frac{\nabla P}{\rho} - \nabla\Phi = 0 \tag{1.4}$$

where υ is a velocity, P is a total pressure, ρ is a density, Φ is a gravitational potential, the Eddington limit defined by the condition:

$$\nabla\Phi = \frac{\kappa}{c} F_{rad}, \tag{1.5}$$

where κ is the opacity, c is the speed of light F_{rad} is the radiation flux, which is connected to the luminosity as:

$$L = \int_S F_{rad} dS, \tag{1.6}$$

which in turn is the luminosity of a source enclosed by a surface S.
Integrating, we obtain the Eddington luminosity:

$$L_{Edd} = \frac{4\pi GMc}{\kappa}, \tag{1.7}$$

where M is the stellar mass.
If L in a given layer approaches L_{edd}, a layer would try to readjust its structure to maintain the hydrostatic equilibrium.

1.3. Outer Layers and Stellar Wind of Massive Stars

While the conditions in the core set the evolutionary stage of a star and its final fate the conditions in the outer layers define how a star appears to an observer. This is also where numerous hydrodynamic instabilities can occur (e.g. convection, pulsations, etc.).
The stellar envelope can be qualitatively defined as the low density low temperature outer region of a star where the recombination of some elements takes place (Grassitelli 2016).

1.3.1. Structure of Outer Layers

The outer layers of massive stars are found to be convective. However, the cause for it is different from the one that is responsible for the convection in their cores and inherently connected to the increase in opacity[2].
As temperature decreases with increasing radius, at a certain point partial recombination occurs of certain elements. Most notably are:

- at $T \approx 160000$K or $\log(T) \approx 5.2$ the iron group elements starts to recombine which increase the opacity in the layer with this temperature, creating the so-called "Iron opacity bump" or IOB,
- at $T \approx 40000$K or $\log(T) \approx 4.6$ the helium undergoes partial recombination with single electron, creating the "HeII opacity bump" or HOB.
- at $T \approx 16000$K or $\log(T) \approx 4.2$ the helium becomes neutral leading to the "HeI opacity bump".
- at $T \approx 8000$K or $\log(T) \approx 4.0$ the recombination of hydrogen creates the "H opacity bump".

This increase in opacity allows for the criterion for convection (Eq. 1.1) to be fulfilled in the outer layers. However, if it occurs relatively close to the surface, where density is low and convection is non-adiabatic and inefficient, the convection fails to transport the required energy flux. This brings the local luminosity L close to the maximum amount of energy that can be transported via radiation, the Eddington luminosity L_{Edd} with important implications for the structure and appearance of a star.

1.3.2. Inflation

In an attempt not to exceed the Eddington limit and preserve the hydrostatic equilibrium, the density gradient in the outer layers of massive stars flattens. As opacity depends on the density, its gradient becomes shallower as well. As a result an extended low density region is formed. This phenomenon is called **inflation** and is caused by the outer layers of massive stars being close to the Eddington limit. This manifests the key importance of the Eddington limit for the structure of the outer envelope of massive, luminous stars (Joss et al. 1973, Sanyal et al. 2015).
Note, that differently from envelope inflation there is a physical process that is sometimes being confused with it. A post-main sequence star with a shell hydrogen burning follows the mirror principle, which is, the expansion of the envelope alongside the contraction of the core (Kippenhahn and Weigert 1994).
Envelope inflation instead can be defined as the formation of an extended, very dilute stellar envelope in which the luminocity is very close to the Eddington one for large regions of space. (Sanyal et al. 2015, Gräfener et al. 2012b,a, Grassitelli et al. 2018, Petrovic et al. 2006). The inflated layers are unstable to convection and turbulence (Grassitelli et al. 2016a,b). It was argued that the extend of an inflated region depends on the applied mass loss rate (Petrovic et al. 2006, Grassitelli et al. 2018), as well as metallicity rotation and the efficiency of convection.
It was shown (Grassitelli et al. 2018), that the outer layers of inflated helium stars exhibit an inflection point at which the value of $d^2\rho/dr^2$ changes the sign, or equivalently:

$$\frac{d\ln(\kappa)}{d\ln(T)} \leq 1 - \frac{1}{\Gamma} \tag{1.8}$$

[2]Here, by opacity the Rosseland mean opacity is implied which is an average opacity, harmonically weighted over the temperature derivative of the Planck curve.

where, κ is an opacity, T is a temperature, Γ is an Eddington Factor.
For more discussion on the envelope inflation see Appendix B.
The formation of these turbulent, poorly bonded, low density layers affects the observed surface temperature of ,assive stars and it is closly related to the appearance of instabilities such as pulsations (Grassitelli et al. 2016a), as well as mass-loss rates by stellar winds.
As the density keeps declining with radius, at some point the radiation becomes free to leave a star. Being thermalized in the stellar interior, it exhibits a blackbody spectrum. However, atoms of certain elements near the stellar surface, that have already partially recombined, absorb some of the outflowing photons, adding an absorption component to the blackbody spectrum. Shape and strength of the absorption lines indicates the relative abundances and the ionization states of different ions in addition to providing information on the surface temperature (Gray 2005).
Many important physical parameters can be inferred from the spectral analysis, such as surface gravity, surface pressure, mass-loss rate and projected surface rotational velocity. The shape and shift of absorption lines are mostly defined by the broadening, which is, in addition to natural quantum mechanical mechanisms, caused by: particle collisions (pressure broadening), electric fields (Stark broadening) and velocity distribution, (thermal broadening).
The atmosphere and spectra; appearance of stars, especially massive stars, is also affected by their stellar winds. In fact, similar to the sun, all stars lost mass from their surface. The rate at which stars lose mass ca vary by several orders of magnitude, depending mostly on the luminosity and temperature, with moreover important implications for their evolution.
Massive luminous stars have radiation-pressure-driven winds (Nugis and Lamers 2002a). In addition, magnetic fields and rotation can contribute (Lamers 2004).
In radiation driven winds the momentum to drive outflows is provided by the interaction between radiation and medium, i.e. momentum redistribution via Coulomb coupling (Lamers and Cassinelli 1999, Braginskii 1965). The high observed mass-loss rates of luminous stars are attributed to the outer layers of massive stars being close to the Eddington limit, and thus poorly bounded to the star, while being subjected to intense radiative fluxes (Langer 2012). In the ultimate scenario, the mass loss can strip a star of the H-rich envelope, leaving a naked helium core.

1.4. Evolution of Massive Stars

Historically, stars' magnitudes and colors were first observed and analyzed. Distributing stars according to these two values on a diagram allowed for a simple classification, that is still used today. In theoretically orientated literature, the luminosity, which is an absolute magnitude, is usually plotted against the effective temperature. Effective temperature for most stars can be understood as a surface temperature, which in turn is related to the color.
The diagram that relates effective temperature and luminosity (or equivalently stellar spectral class and magnitude) is called Hertzsprung-Russel diagram (HR diagram or HRD). An example of HRD is shown in the Figure 1.1. The diagram displays various stellar types. Stars populate different parts of the HR diagram depending on their chemical composition stellar mass and stage of evolution.
Life of a star can be seen as a continuous contraction interrupted by long-lasting phases of nuclear burning. During the Main Sequence, a star is burning hydrogen in its core. During this phase stars occupy a transversal band in the HRD (see Fig. 1.1) and this is the phase in which stars spend $\sim 90\%$ of their lives.
Low mass $M < 0.5 M_{\odot}$ are fully convective and burn hydrogen via pp-chain set of reactions. These stars are cool and not very luminous and, thus, located in the bottom right corner of the figure 1.1.
Massive stars have convective cores and radiative envelopes. They burn hydrogen via CNO chain of nuclear reactions, which proceeds at higher temperatures and densities. The large energy output places these stars in the upper-left part of the HRD.

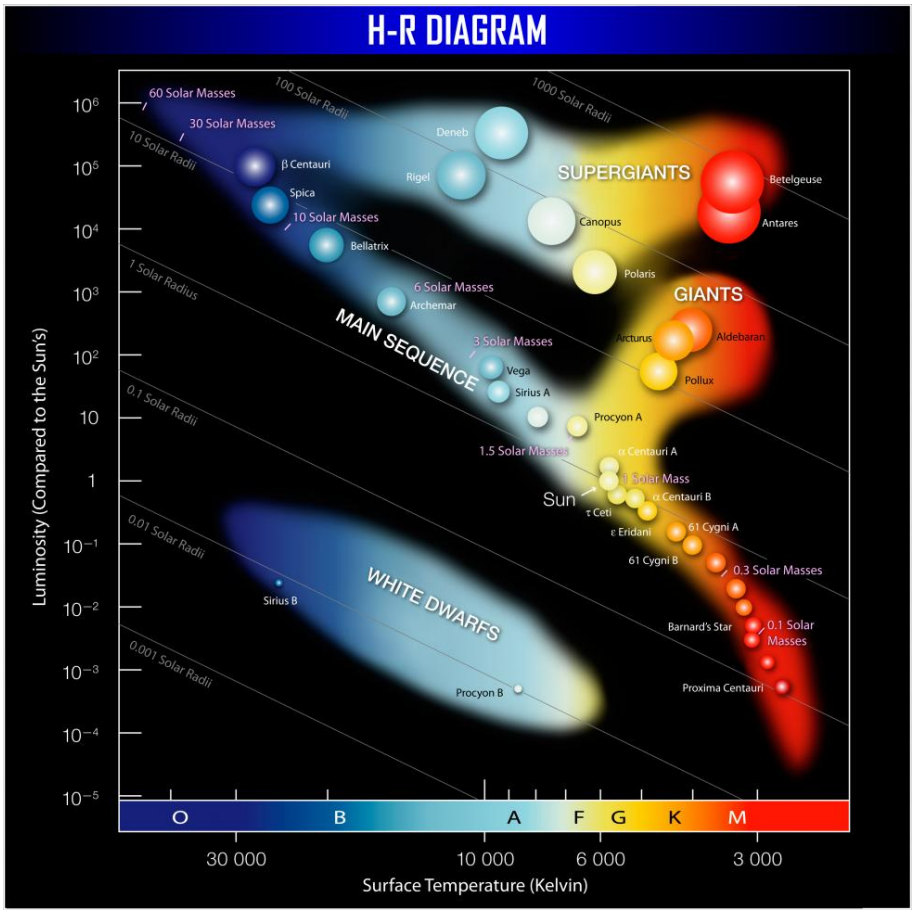

Figure 1.1.: HR Diagram. Credit: ESO

1.4.1. Core evolution of massive stars

After the hydrogen exhaustion in the core, it contracts until the temperature and density are high enough for helium ignition.

After the helium is exhausted in the core, it starts to contract once again, until carbon is ignited[3], after that neon, then oxygen. This step-like process continues until the iron is synthesized in the core. Iron has the highest binding energy per nucleon, which means that its fusion into heavier elements is an endothermic process. While core continues to contract, the temperature reaches $\sim 10^9$K and photons become energetic enough to disintegrate recently formed iron nuclei, splitting them into the lighter ones. As photons get absorbed in this process, the radiation pressure that was supporting the core, drops, which lead to a rapid violent collapse. At certain values of density and temperature, protons start to capture free electrons transforming the core into a giant nucleus composed on neutrons. Neutrons are fermions, and the Pauli Exclusion principle can stop the collapse leaving behind a neutron star. However, if the mass of the core is too large, the collapse continues until the Schwarzschild radius is passed, which constitutes the formation of a black hole. Regardless, this is the end of the core evolution.

[3] in this description shell burnings are neglected for the sake of simplicity

1.4.2. Wolf-Rayet Stars

Massive luminous (million times more luminous than Sun) stars in the late stages of evolution, embedded in a optically thick, dense winds, displaying emission lines in their spectra are called **Wolf-Rayet stars** (Crowther 2007).
WR stars exhibit the highest steady state mass-loss rates of order of $\sim 10^{-4} M_{\odot}/\mathrm{yr}$, caused by the proximity of the outer layers to the Eddington Limit, and radiation driven stellar winds, enhanced by multiple scattering and progressive Doppler shift, that reduces the effect of line-blanketing (Lamers and Cassinelli 1999).
Observed effective temperatures of WR stars varies from $\sim$ 30000K for late type WN9h stars to $\sim$ 200000K for early type WO stars. WN stars have effective temperatures in rage $\sim$ 30000K for late type WNh to $\sim$ 141000K for early type WN stars. Luminosities varies from hundreds of thousands to several million solar luminosities. Thus, these stars are located in the upper-left corner in the HR diagram. There are about 500 Wolf-Rayet stars discovered in the Galaxy and around 150 in the Magellanic Clouds (Crowther 2007, Schaerer et al. 1999).
Observations showed the presence of inhomogeneities within winds, such as clumps (Moffat et al. 1988), and porosity (Oskinova et al. 2007).
The WR stars show a characteristic profile in the spectra, called P Cygni profile. It appears if a given emission line, formed in the rapidly moving wind, 'merge' with Doppler shifted absorption line. This profile, if observed, allows for the estimation of the mass-loss rate $\dot{M}$ and the terminal velocity of the wind v_{∞}, which is the velocity at a radius, where the acceleration is ceased.
The radiation, emitted is directed back to the star by the dense wind, giving rise to a back-warming of the outer hydrostatic layers which is proportional to the optical depth.
Wolf-Rayet stars are usually classified based on the emission line strengths and line ratios of certain elements (Crowther 2007):

- WN stars with spectra dominated by helium and nitrogen emission lines,
  - WNL (WNh) stars with Hydrogen present at the surface, and are believed to be still core hydrogen burning,
  - WNE stars with no hydrogen detected in the spectra, and are believed to be core helium burning stars,
- WC stats with carbon lines being prominent in the spectra,
- WO stars with Oxygen lines being prominent in the spectra.

From here on we will focus on the WNE class, which is further divided into subclasses, following a scheme that involves line ratios of N iii-v and He i-ii, ranging from WN2 to WN5 for "early WNE" stars, and WN7 to WN9 for "late WNE" stars (Crowther 2007). In addition, if WN has a weak emission lines it is classified as "WN-w", if the lines are strong, – "WN-s" (Hamann et al. 2006). The Shape of the lines also differ, as the week lines originate from rapidly accelerated material close to the core, the WNE-w have triangular shaped lines, while WNE-s have more common, Gaussian lines (Crowther 2007).
Being one of the prime sources of ionizing radiation, Wolf-Rayet stars had an influence on the cosmic reionization (Lu et al. 1998), and in turn, on galaxy formation. On smaller scales, WR stars are one of the most luminous objects, affecting the spectroscopic appearance of the host galaxy, or even dominating it (Schaerer et al. 1999), and enriching the interstellar medium with nuclear-processed material (Draine 2011). In single star evolution, it has been suggested that WR phase lies on the evolutionary path of massive O stars that can include LBV (Meynet and Maeder 2003) which are also not fully understood, but believed to have a similar conditions in their envelops

(Gräfener et al. 2012a). A better understanding of the WR phase would result in a more accurate binary evolution models where the hydrogen rich envelop of one of the component is removed in the common envelope phase (Taam and Sandquist 2000). The statistics of Wolf-Rayet stars provides an additional constraint on the theory of star formation and evolution, that can benefit to the accuracy of population synthesis. More importantly, WR stars are the direct progenitors of Supernovae (Yoon and Langer 2005), producing the most massive compact objects, black holes (Heger 2013), and Gamma-ray bursts (Cui et al. 2010). The very rapidly developing field of gravitational wave (GW) astrophysics (Abbott et al. 2016, 2017), especially the formation of GW progenitors, would benefit considerably from a better understanding of WR phenomena.

1.5. Statement of the problem and Previous Works

Problem Wolf-Rayet stars have optically thick, dense winds with the photosphere lying in the supersonic part of the outflow. Thus, the base of the wind is veiled from the observations. It was pointed out, that there is a disagreement between the between the empirically determined hydrostatic radii of WR stars (Hamann et al. 2006, Hainich et al. 2014) and the radii inferred from stellar structure calculations (Langer 1989, Gräfener et al. 2012b). This disagreement is called "Wolf-Rayet Radius Problem". Reaching almost an order of magnitude, it presents a challenge for the understanding of the structure of massive stars.
Additional factor, contributing to this problem is the complex subsonic structure, that can include inflation and density inversion (Sanyal et al. 2015). Moreover, numerical models suggests that the exact configuration of the subsonic layers, as well as the mechanism that accelerates the flow to the transonic velocities, depend on the applied mass-loss rate (Petrovic et al. 2006, Grassitelli et al. 2018).
The second aspect of the "Wolf-Rayet radius problem" is the observed variety of spectral subtypes of Galactic WNE stars with different photospheric temperatures but with the same luminosities. However, from Langer (1989), the properties of these stars are expected to be mostly defined by one single parameter, their luminosity.

Previous Works The WR radius problem has been investigated by multiple groups. After the introduction of the OPAL opacity tables (Iglesias and Rogers 1996), into the stellar structure models, the formation and structure of inflated, low density, extended envelopes were thoroughly investigated (Langer 1997, Gräfener et al. 2012a,b, Sanyal et al. 2015, 2017, Grassitelli et al. 2016a, Petrovic et al. 2006, Grassitelli et al. 2018, Nakauchi and Saio 2018, Gräfener et al. 2017).
In addition, attention was given to the emergence of so called pseudo-photospheres, which lies high above the hydrostatic domain and are caused by the optically thick, dense outflows of these stars (Crowther 2007).
In contrast to applying pre-imposed velocity structures (instead of solving the momentum equation) in the wind, sophisticated 1D radiation hydrodynamic simulation of the structure of envelopes and the atmospheres of Wolf-Rayet stars were constructed (Gräfener and Hamann 2005).
The structure of the layers that are close to the Eddington limit ($\Gamma = L/L_{Edd} \approx 1$) sensibly depends on the opacity, and recently it was suggested that, in the vicinity of the iron opacity peak, the opacities are higher by 75% than OPAL provides (Turck-Chièze et al. 2016). This is especially important in light of the more recent work, where it was pointed out that at the point where the mass-loss rate is set, the sonic point, a relation exists between opacity, density, and temperature, based on OPAL tables. Under the assumptions of LTE at that point, which is justified if the optical depth is large, and assumption regarding the sonic radius, the model-independent sonic point conditions for observed WNE stars can be inferred, based on their L/M and $\dot{M}$ (Grassitelli et al. 2018). It was suggested that all Galactic WNE stars have the same mechanism of wind

acceleration to transonic velocities, namely, momentum input provided by the increase in opacity in the vicinity of the iron opacity bump. The sonic point temperatures of Galactic WNE stars were shown to be distributed homogeneously, following A sonic point temperature – luminosity relation. However, the reason for a still present degree of scatter, as well as the interplay between sonic point temperature and photospheric conditions of Galactic WNE star, are not clear.

This work We analyze the sonic point conditions of the Galactic and LMC H-free WNE stars. Combining this with the analysis of the relation between the hydrostatic and photospheric conditions and our own models, we investigate the conditions at the base of the winds of massive helium stars models at different metallicities and at different evolutionary stages. We investigate the parameter space (in terms of L/M, $\dot{M}$, Z, chemical composition) of the observed early-type WN stars, based on newly computed stellar structure and evolution calculations as well as model-independent theoretical tools. Such an analysis is performed while taking into account the latest state-of-the-art observations available from the literature.
This analysis includes the uncertainty on the observed parameters, such as luminosity and mass-loss rate; the evolutionary stage of these stars, metallicity and the photospheric conditions.

Chapter 2.

Theoretical Concepts

2.1. Theoretical concepts

2.1.1. OPAL opacity tables & Optical Depth

The interaction between radiation and matter is a complex process involving absorption of line photons, scattering, recombination; affected by the line broadening, and depends on many physical parameters of the radiation field as well as the medium (Lamers and Cassinelli 1999). In order to simplify the description of this interaction, the mean opacity averaged over all wavelengths, or the Rosseland mean opacity, was introduced:

$$\frac{1}{\kappa} = \frac{\int_0^\infty \frac{1}{\kappa_\nu} \frac{\partial B_\nu(T)}{\partial T} d\nu}{\int_0^\infty \frac{\partial B_\nu(T)}{\partial T} d\nu}, \tag{2.1}$$

where B_ν is a spectral radiance.
By studying gases with different chemical composition, tables were computed where the Rosseland opacities are computed as a function of density and temperature (taking into account the atomic properties, such as energy levels, oscillator strengths and photoionization cross sections) (Berrington 1995, Iglesias and Rogers 1996).
These tables are implemented into modern stellar evolution codes. The graphical representation of these tables for helium gas with Galactic and LMC metallicities is shown in the figure 2.1.
From figure 2.1 it is seen that at fixed temperature the opacity increases with density. At a fixed density, starting form the low temperatures there is a rapid rise in κ associated with ionization of He. The peak in opacity around $10^{4.6}$K is related to the helium becoming fully ionized, the final peak around $10^{5.2}$K (Fig. 2.1) corresponds to the partial ionization of the iron-group elements and its strength strongly depends on metallicity.
Despite the convenience and simplicity that Opacity tables provides, it is important to remember that they represent an approximate relations for static medium. In case of moving gas, additional effects become important for the interaction between radiation and matter, such as Doppler effects and line deshadowing.

Optical depth is an integral measure of an extinction coefficient or absorptivity over a given length. It describes the attenuation of the radiation, as it passes through a defined length in the medium (Draine 2011). Expressed in terms of Rosseland mean opacity it is

$$\tau = \int_z^\infty \frac{ds}{\mu'}, \tag{2.2}$$

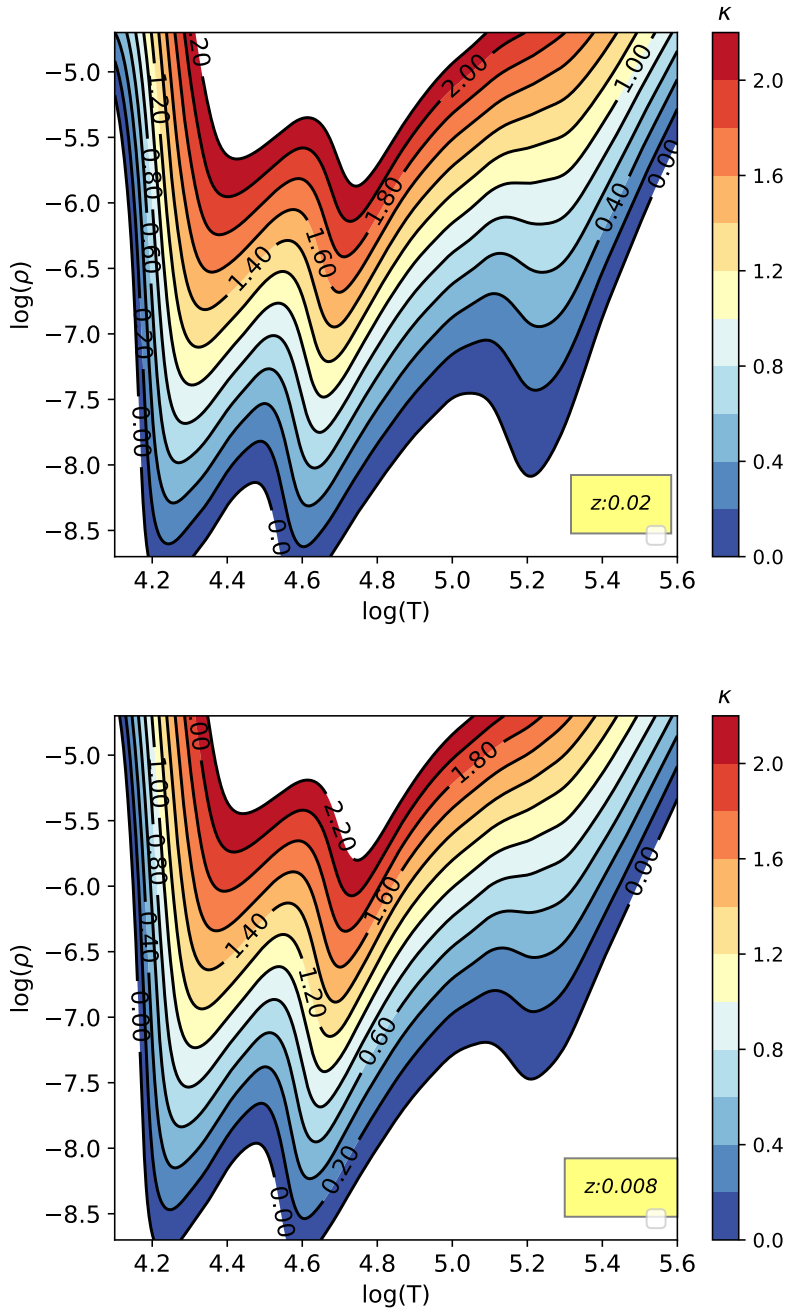

Figure 2.1.: Opacity tables (Iglesias and Rogers 1996), where the Rosseland mean opacity ($\kappa/cm^2/g$) is plotted against the temperature ($\log(T/K)$) and density ($\log(\rho/g/cm^3)$), where the opacity is colourcoded. Top table is for the gas with ($X = 0, Y = 0.98, Z = 0.02$) chemical composition, and bottom table is for ($X = 0, Y = 0.99, Z = 0.008$), that correspond to average Galactic and Large Magellanic Cloud respectively. Interpolation is done via smooth interpolated univariate spline of third order.

where z is a coordinate up to which, going from infinity, the optical depth is evaluated, τ is the wave-length independent optical depth, μ' is an extinction coefficient.

The optical depth, as it follows from Eq. 2.2, decreases with radius. Regions with $\tau > 2/3$ are said

to be optically thick, while $\tau \leq 2/3$ indicates an optically thin region. At the point where $\tau \leq 2/3$ the radiation is assumed to become free, and in the stellar atmosphere it constitutes the location of the wave-length independent (gray) photosphere.

2.1.2. Radiation Driven Winds

The winds of Wolf-Rayet stars are radiation-pressure-driven (Nugis and Lamers 2002a). This means, that the momentum to accelerate the flow is provided by the continuum radiation absorbed and scattered in a optically thick medium. The absorbed momentum is then efficiently redistributed withing the flow via Coulomb coupling.
The momentum equation for the steady-state stellar wind is

$$\frac{1}{\upsilon}\frac{d\upsilon}{dr} = -\left(g - g_{rad} - 2\frac{\upsilon_s^2}{r} + \frac{dc_s^2}{dr}\right) \cdot \frac{1}{\upsilon^2 - \upsilon_s^2} \tag{2.3}$$

where g is the gravitational acceleration, g_{rad} is the radiative acceleration, υ_s is the local isothermal sound speed, υ is the flow velocity, and r is the radial coordinate.
Here, the radiative acceleration is defined by

$$g_{rad} = \frac{\kappa L}{4\pi r^2 c} \tag{2.4}$$

where κ is the Rosseland mean opacity from Thompson scattering and from bound-bound and bound-free absorption, which is assumed in this context to be consistent with the flux-weighted mean opacity, G is a gravitational constant and c is a speed of light.
The equation 2.3 implies that in order to achieve a smooth transonic flow, the $d\kappa/dr > 0$. The increase in opacity provides the momentum to drive the wind.
Withing the assumption of local thermodynamic equilibrium at the sonic point, which is justified by the high optical depth (Nugis and Lamers 2002a), the macroscopic parameters, such as temperature can be defined by local quantities only. The isothermal sound speed can be evaluated as

$$\upsilon_s = \sqrt{\frac{k_B T}{\mu m_H}}, \tag{2.5}$$

where μ is the mean molecular weight, m_H is the mass of a hydrogen ion, and k_B is the Boltzman constant.
Here we assume that the opacity κ does not depend on the velocity gradient, of equivalently, that the Doppler effect is negligibly small. This in turn, allows to use OPAL opacities to evaluate g_{rad}. Models showed that this is a good approximation in the subsonic part of the flow, however in the supersonic part, the $d\upsilon/dr$ increases rapidly and solving the equation 2.3 becomes much more difficult, in particular, evaluation of opacity. In this case, the radiative transfer and hydrodynamics has to be modeled simultaneously. Alternative to that, is to use the pre-imposed velocity (and density) profile, namely the β-law is used (Lamers and Cassinelli 1999).
The the β-law is defined as following,

$$\upsilon(r) = \upsilon_\infty\left(1 - \frac{r_s}{r}\right)^\beta \tag{2.6}$$

where r_s is the base of the wind and υ_∞ is a terminal velocity, the velocity at large radius, where acceleration is ceased.
Or as

$$\upsilon(r) = \upsilon_s + (\upsilon_\infty - \upsilon_s)\left(1 - \frac{r_s}{r}\right)^\beta \tag{2.7}$$

to avoid the $\upsilon = 0$ at the sonic point (Langer 1989).

2.1.3. Sonic Diagram

In a recent work, Grassitelli et al. (2018), it was shown that the outer layers of helium star models are close to the local Eddington limit ($\Gamma_s \approx 1$). In addition, it was shown that the radiation field at the sonic point of Galactic WNE stars is close to LTE. These arguments allow to design a tool for the estimation of hydrostatic parameters of WNE stars.
The method is based on two main relations: the validity of the opacity tables at the sonic point and the adoption of the relation between opacity and L/M ratio, if $\Gamma_s = 1$, namely:

$$\kappa_E = 4\pi cG(L/M)^{-1}, \tag{2.8}$$

where κ_E is the Eddington opacity, L is the stellar luminosity, M is the stellar mass, c and G hold their usual meaning, and the continuity equation

$$\dot{M} = 4\pi R_s^2 \rho_s \upsilon_s \tag{2.9}$$

where ρ_s is the density, υ_s is the velocity and R_s is the radius at the sonic point.
The opacity tables relate opacity κ as a function of temperature T and density ρ (Fig. 2.1). They can be inverted to estimate the ρ as a function of T and κ, which is shown in the figure 2.2, top panel. Obtained relation $\rho = f(T, \kappa)$, combined with equations 2.8 and 4.1 result in a relation between L/M, T_s and $\dot{M}$. However, in doing so, the sonic radius R_s and mean molecular weight μ have to be assumed for the equation 4.1. The result is shown in the figure 2.2, bottom panel. This diagram is called The Sonic Diagram (SD). As the contours of constant mass-loss rate behave monotonically in the hot part of IOB, it allows from known L/M and $\dot{M}$ to estimate the sonic point temperature. This is done for Galactic WNE stars in (Grassitelli et al. 2018), with the assumed $R_s = 1.0R_\odot$ and $\mu = 1.34$.
From figure 2.2 (bottom panel) it follows that, for a constant L/M, if mass-loss rate is decreasing so does the sonic point temperature. When temperature approaches $\log(T) \propto 5.20$, this trend stops. This is because the $d\kappa/dr$, which is > 0 in the hot part of the iron opacity bump, when $\log(T) > 5.20$, is not longer present. The $\log(T) \propto 5.20$ is a peak of IOB, after which (in terms of temperature) the $d\kappa/dr < 0$. Thus, if the flow was not able to reach the sound speed before $d\kappa/dr$ changes the sign, it decelerates. The mass-loss rate, lower than which this happens is called the critical mass-loss rate M_{cr} (Grassitelli et al. 2018).
Notable, the condition $d\kappa/dr > 0$ is present in the hot part of every opacity bump. Thus, the flow that has failed to pass the sonic point in the hot part of Iron opacity bump, can succeed in the vicinity of the Helium II opacity bump.

2.2. Note on the Observed WNE stars

2.2.1. Galactic WNE stars

In this section we introduce the observational data.
The comprehensive analysis on the Galactic Wolf-Rayet stars of the nitrogen sequence was done by Hamann et al. (2006). Among 127 stars analyzed in there, we select a subset of 31 H-free WNE stars.
The physical parameters of these stars where evaluated via computing models of stellar atmospheres and fitting the observe spectra to the synthetic one. The atmosphere models used by Hamann et al. (2006) included effects of non-LTE physics and their super- sonic expansion and the line blanketing by the millions of lines from iron and iron-group elements. From the model fitting, authors estimate

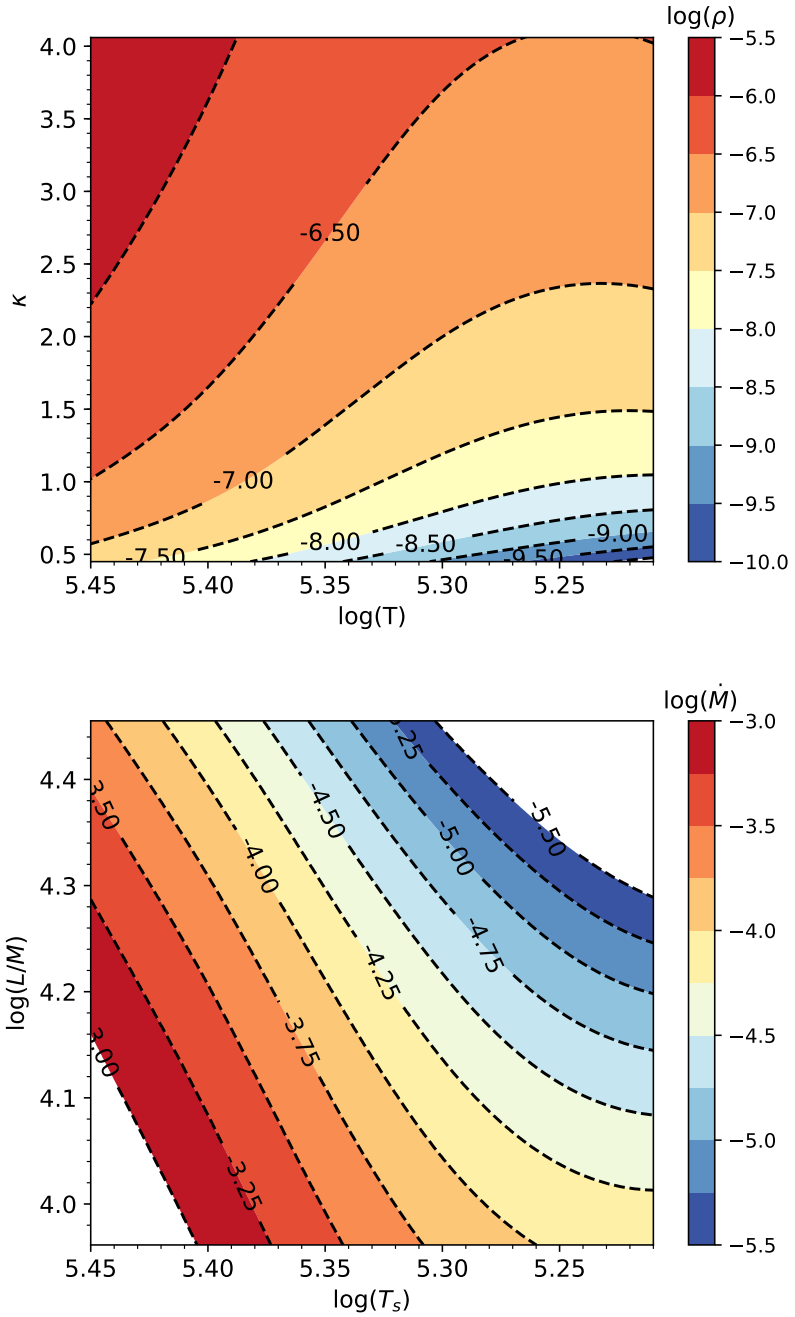

Figure 2.2.: Top panel: hot part of the iron opacity bump with the opacity plotted as a function of temperature $\log(T)$) and density $\log(\rho)$, where the latter is color-coded. The relation is obtained by inverting the matrix of OPAL table (Iglesias and Rogers 1996). The region corresponds to the hot part of the iron opacity bump. Bottom panel: Sonic Diagram (SD) that relates the $\log(L/M)$, sonic point temperature $\log(T_s)$ and mass-loss rate $\log(\dot{M})$, where the latter is color-coded. Both panels are for the Galactic metallicity

the following parameters of a star, the T_* and R_t. The T_* is a temperature of the model at high optical depth, $\tau = 20$, that is considered to be deep withing the hydrostatic domain. The R_t is a transformed radius, which is defined as

$$R_t = R_* \left[\frac{\upsilon_\infty}{2500 \text{ km/s}^{-1}} \Big/ \frac{\dot{M}\sqrt{D}}{10^{-4} M_\odot \text{yr}^{-1}} \right]^{2/3}, \tag{2.10}$$

where R_* is the radius at $\tau = 20$, υ_∞ is the terminal velocity, D is the clumping factor, that accounts for inhomogeneities, clumps, in the stellar wind.
In this sophisticated method it is hard to provide and error bar. Authors suggested a ± 0.1 for the $\log(R_t)$ and $\log(T_*)$, similar to the adopted the later works (Sander et al. 2012). The error bar on the luminosity is also difficult to evaluate as the distance towards most of the single Wolf-Rayt stars cannot be measured directly[1] and usually inferred from the cluster associations. Following Gräfener et al. (2017) we adopt ± 0.2 for $\log(L)$. Similarly we adopt ± 0.15 for the $\log(\dot{M})$
Within the WNE class, the stars are further subdivided with respect to their relative line strength, which in turn is set by the temperature in the photosphere. The WN2, the early WNE, are the hottest and the late WN8 is the coolest among the Galactic WNE. These stars cover a broad parameter space, approximately $\log(L/L_\odot) \in (5.2, 6.2)$ and $\log(\dot{M}) \in (-5.4, -4.)$ (see Fig. 2.3, top panel).
One of the results of spectral fitting analysis is shown on the bottom panel of the figure 2.3, where T_* covers also a broad range $\log(T_*) \in (4.5, 5.2)$. Meanwhile the stellar evolution models of core helium burning stars predict $\log(T) \propto 5.$ at the surface. This is the previously described Wolf-Rayet Radius problem.

2.2.2. LMC WNE stars

The observational data for H-free WNE stars in Large Magellanic Cloud have been analyzed by Hainich et al. (2014). One of the results is shown in the figure 2.4.
The WNE stars in LMC show overall lower mass-loss rates $\log(\dot{M}) \in (-5.6, -4.4)$ and lower luminosities $\log(L/L_\odot) \in (5.2, 5.8)$. In addition, their luminosities have lower error bar (± 0.1), as the distance to the Large Magellanic Cloud is better constrained. For the mass-loss rate we adopt same error as in the Galactic WNE, following the Gräfener et al. (2017).
The variety of spectral subtypes is smaller in LMC, as the WN4 is the latest WNE present. However, there are hot early-type WN2 stars which we discuss in more details in the results.
Similarly to the Galactic WNE, there is a discrepancy between the T_* and the perditions from the stellar structure models, however, it appears to be less prominent, as $\log(T_*) \in (4.8, 5.2)$.

2.3. Photospheric Parameters

The photospheric conditions (at $\tau = 2/3$) are not directly available in the Hamann et al. (2006), Hainich et al. (2014). In order to extract them, we perform the following procedure. Collecting the data regarding the computed WNE atmosphere models from a website `http://www.astro.physik.uni-potsdam.de/~wrh/PoWR/powrgrid1.php`, we construct a relation between the transformed radius R_t, temperature T_* and the T_{eff}, which is a temperature at the photosphere.
This relation, shown in the figure 2.5, allows to estimate the photospheric conditions of the observed WNE stars, using the R_t and T_* provided by Hamann et al. (2006) and Hainich et al. (2014) for the Galaxy and LMC respectively.
The figure 2.5, allows not only to infer the T_{eff} of the model with given R_t and T_*, but also, the error bar on the effective temperature owing to the almost monotonic behavior of the contours of constant effective temperature. Knowing the that uncertainty on the transformed radius and T_*, we take the lower limit of both and compute the T_{eff} for it. Similarly, for the upper limits of T_* and

[1] Recently the GAIA luminosities, obtained from measured parallaxes became available. They are discussed in the Results section.

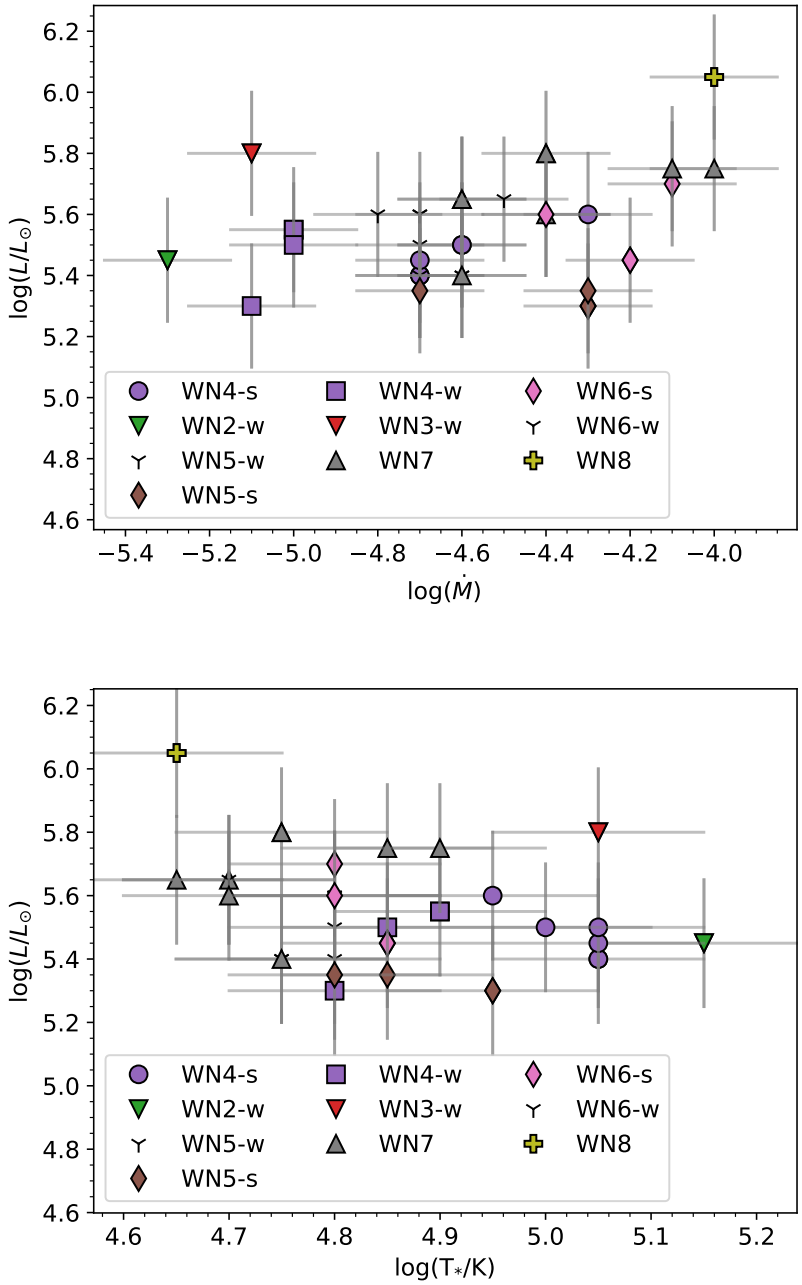

Figure 2.3.: Top panel: Luminosity and mass-loss of the Galactic WNE stars. Bottom panel: T_* and luminosity. Gray lines are the observational uncertainty.

R_t. This method has an important consequence. The size of an error bar on the T_{eff} depends on the stars' position in the Fig. 2.5, as contours of T_{eff} behave non-linearly.

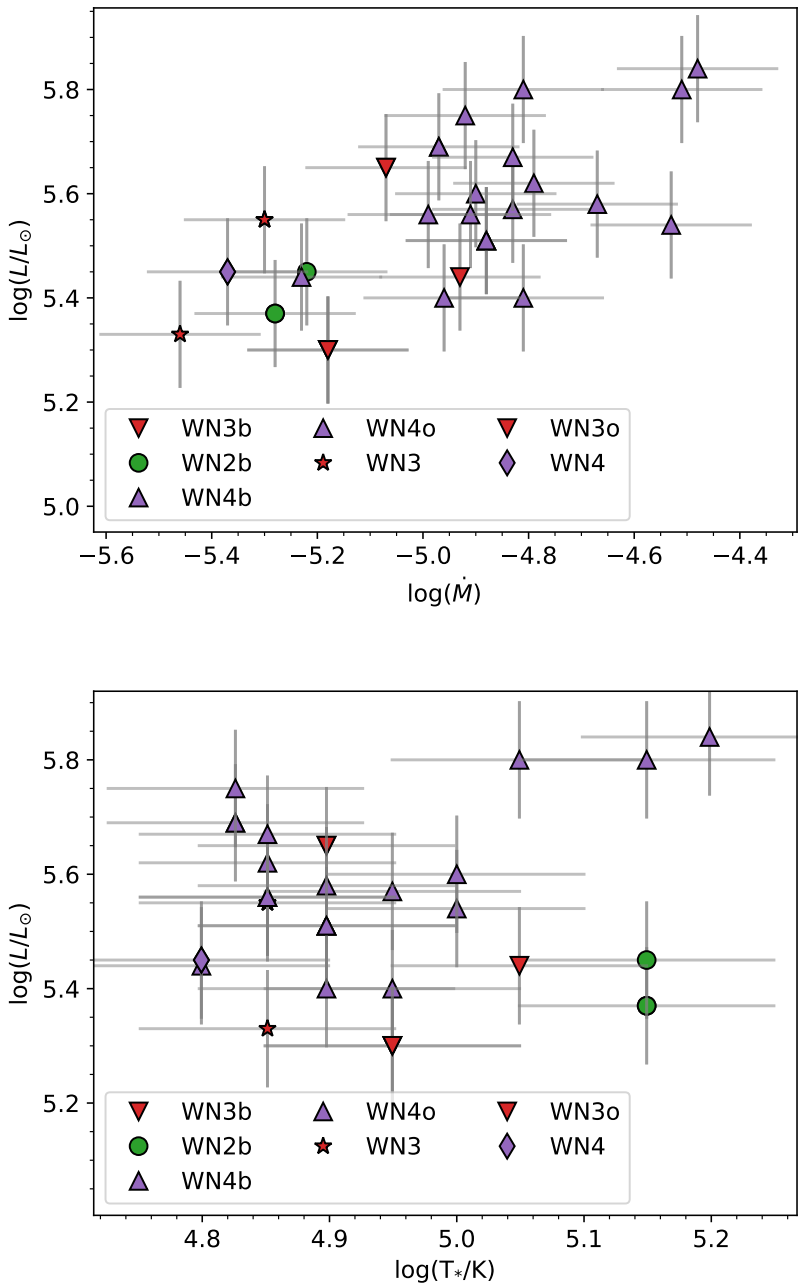

Figure 2.4.: Top panel: Luminosity and mass-loss of the LMC WNE stars. Bottom panel: T_* and luminosity. Gray lines are the observational uncertainty.

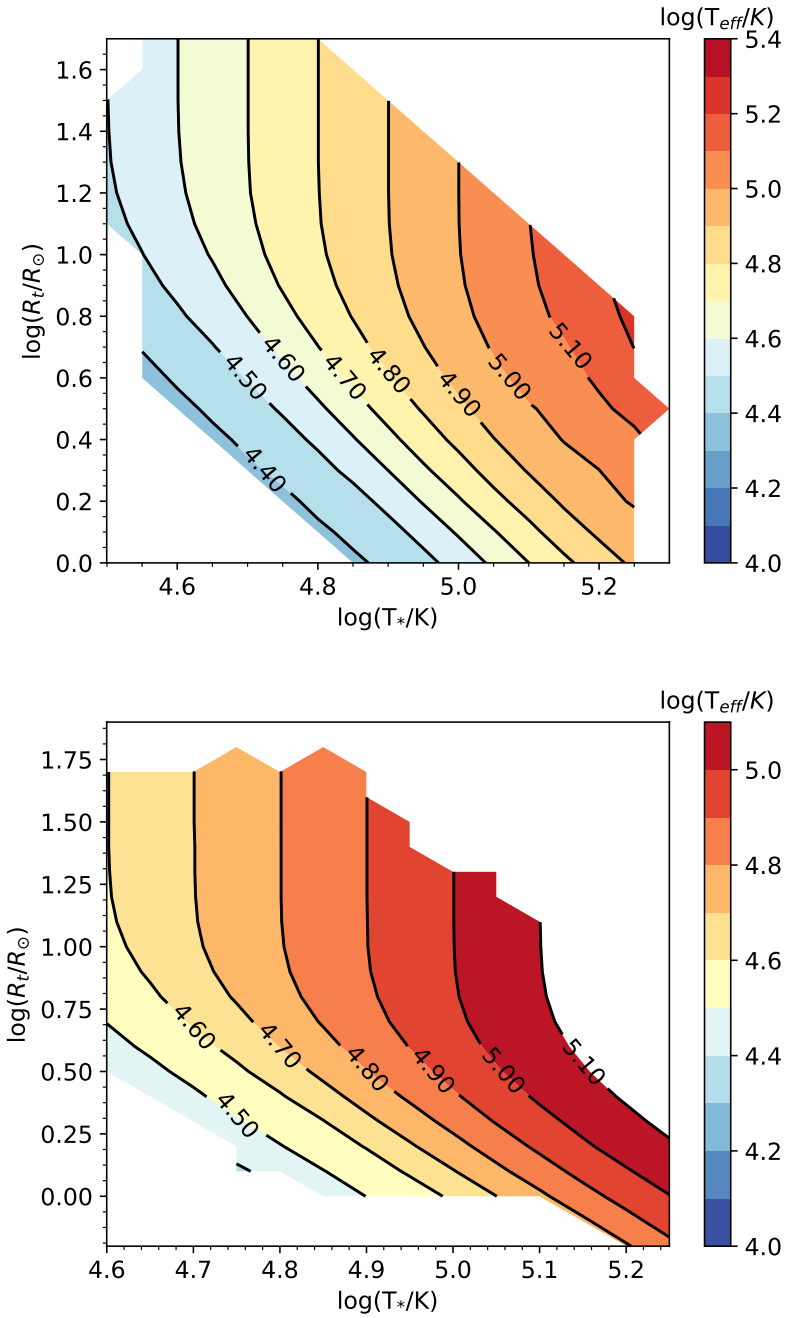

Figure 2.5.: Effective temperature at $\tau = 2/3$, the photospheric temperature, as a function of transformed radius R_t and T_* from models available at `http://www.astro.physik.uni-potsdam.de/~wrh/PoWR/powrgrid1.php` for Galactic (top panel) and LMC (bottom panel) metallicities.

Chapter 3.

Method

In this work we perform stellar structure calculation of helium stars that are believed to the be representative of the WNE class (Langer 1989, Yoon 2017). Our models are computed numerically, solving a hyperbolic set of differential equations simultaneously with well-defined boundary conditions. We employ BEC, which is a Lagrangian hydrodynamic one-dimensional stellar evolution code. The code solves a set of coupled non-linear partial differential stellar structure equations. Combined with the network of nuclear reaction rates, mixing length theory equation set and, based on atomic physics, opacity tables OPAL, they define structure and evolution of a stellar model (Langer et al. 1988, Yoon and Langer 2005, Petrovic et al. 2006). The outer boundary conditions are set at the sonic point while preserving continuity (Grassitelli et al. 2018), or assuming plane-parallel gray atmosphere boundary conditions.
Starting models are chemically homogeneous helium stars with the following composition:

- Galactic metallicity: $X = 0, Y = 0.9815, Z = 0.020$,
- Super-galactic: $X = 0, Y = 0.9615, Z = 0.040$,
- Large Magellanic Cloud: $X = 0, Y = 0.9926, Z = 0.008$,
- Small Magellanic Cloud: $X = 0, Y = 0.9963, Z = 0.004$.

Prior to the analysis these models were relaxed. The hydrostatic and thermal equilibrium were achieved by setting a large time step of order 10^{20} sec, while mass loss and chemical evolution were turned off.
The nuclear burning was realized by means of the state of the art nuclear network. The mixing length parameter was set to 1.5. Overshooting was set to 0.335 with the Schwarzschild criterion for convection. The mass-loss prescription for the chemical evolution of helium models was adopted from (Yoon 2017), defined as.

$$\dot{M}_{WNE} = f_{WR}\Big(\frac{L}{L_{\odot}}\Big)^{1.18}\Big(\frac{Z_{init}}{Z_{\odot}}\Big)^{-0.60}10^{-11.32}, \tag{3.1}$$

where $\dot{M}_{WNE}$ is the mass-loss rate during the WNE phase, f_{WR} is the scaling factor, that accounts for the uncertainty in the empirical estimates of WR mass-loss rates ,Z_{init} is the initial metallicity. Chemical evolution was stopped when the core helium fraction reaches ${}^4He_{core} = 0.1$. From the resulted evolutionary sequence of models, a set has been drown with a ${}^4He_{core} \in [1.0, ..., 0.1]$, where the first value 1.0, corresponds to the He-ZAMS composition, at steps of ${}^4He_{core} = 0.1$.
Considering that strictly speaking the ${}^4He_{core} = 0.1$ is not the end of core helium burning, the thermal and hydrostatic equilibrium is still possible for them. The models at different moment throughout their evolution employed in this study were relaxed to achieve thermal equilibrium via large time-step, while the chemical evolution and the mass loss were turned off.

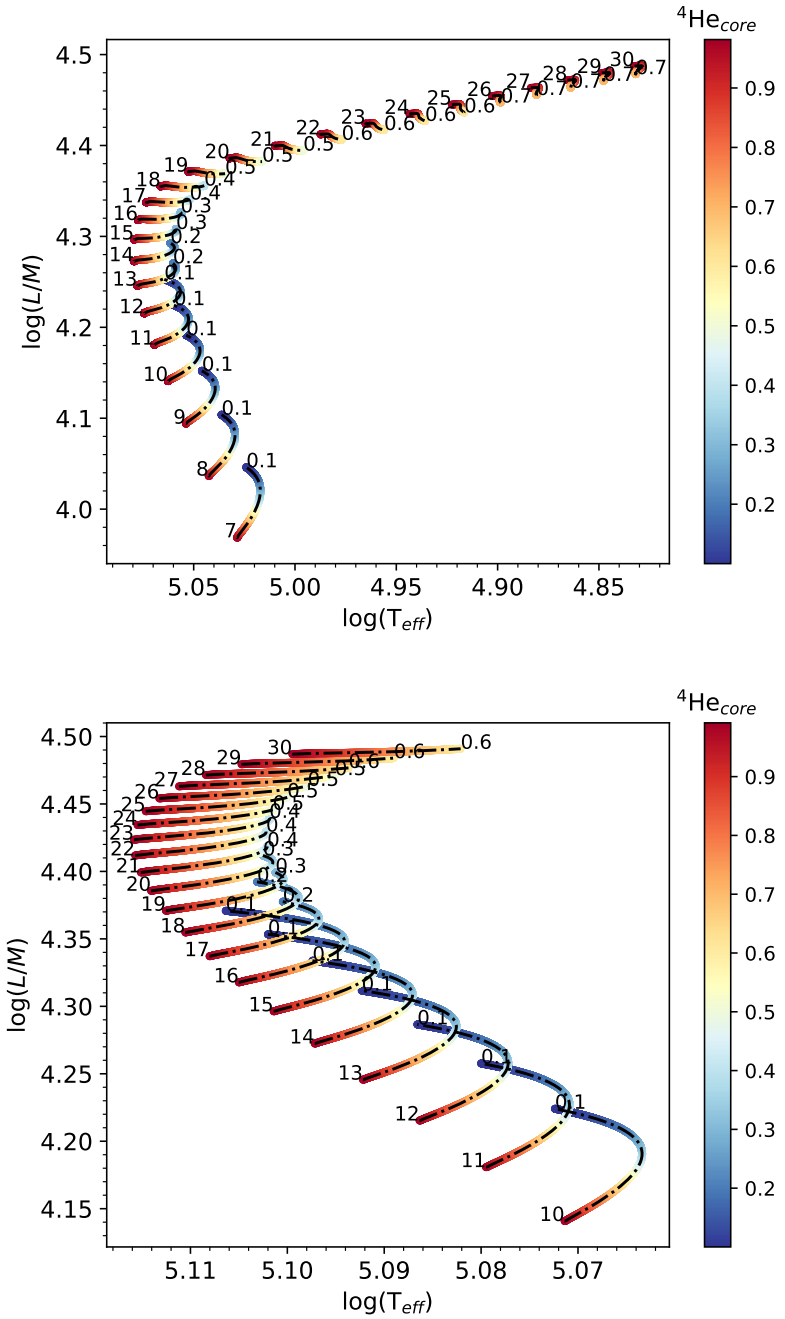

Figure 3.1.: Top and bottom panels are HR diagrams for the stars with Galactic and LMC metallicities. Numbers on the left side of every track are initial masses of the models. Color bar represents the helium content. Evolutionary tracks are limited by the value $^4He_{core} = 0.1$ or by the $^4He_{core}$ at which the change in the surface occurred.

Taking the hydrostatic models with given value of $^4He_{core}$, a set of hydrodynamic models was computed with imposed mass-loss rates in the range $\log(\dot{M}) \in (-3.5, -6.0)M_\odot$ at steps of $\log(\dot{M}) = 0.05M_\odot$ for plane-parallel gray atmosphere models and $\log(\dot{M}) = 0.01M_\odot$ for the sonic point boundary conditions.

Grid of models with the sonic point boundary conditions is used to study the sonic point (T_s, R_s, $etc.$)

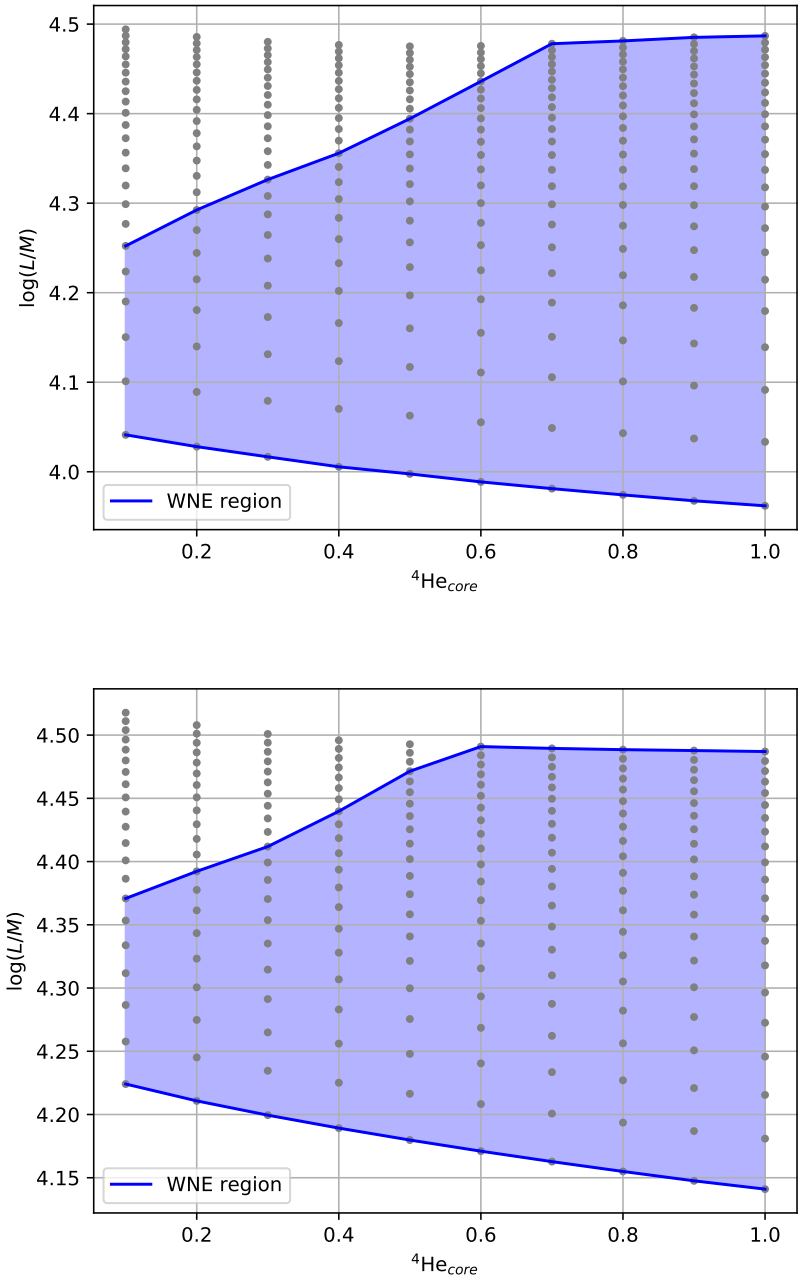

Figure 3.2.: Top panel: grid of stellar models with galactic metallicity, at different evolutionary stages, which is determined by the core helium content ${}^4He_{core}$. The grid includes stars with initial mass $M \in (7-30)M_\odot$ with the step of $1M_\odot$. Bottom panel: grid of stellar models with LMC metallicity, at different evolutionary stages. The grid includes stars with initial mass $M \in (10-30)M_\odot$ with steps of $1M_\odot$. In both cases, the blue colored region encapsulates models with unchanged surface chemical composition, the WNE models.

and photospheric conditions as well as to infer the optical depth at the sonic point τ. The latter is done by computing wind structure on top of the subsonic domain, assuming validity of the

β-law. Using the β-law, (Eq. 2.7) and the continuity equation (Eq. 4.1) we compute the velocity and density profiles for every model with prescribed mass-loss rate. The outer boundary is set at the radius, where velocity reaches the terminal one υ_∞. Integrating over the resulted structure, we obtain optical depth at the sonic point (Eq. 2.2). Assuming the validity of the diffusion approximation in the supersonic part of the flow, we compute temperature at the $\tau = 2/3$, the photospheric temperature.
Together, the subsonic and supersonic structures are used to for the smooth transonic solution. For the detailed explanation, how it is done, see Appendix (D).
For the detailed explanation, how the critical mass-loss rate is estimated, see Appendix (C).
All models, computed with mass loss applied show departure from hydrostatic equilibrium, as there are non-vanishing inertia terms. Time steps of order 10^6 sec were applied to assure the quasi-stationary of the flow, and even for the highest values of mass-loss rate, the decrease in stellar mass did not exceed 1% and it was smoothed out by the following interpolations between models.

3.1. Subsonic structure of helium models

As an example, we discuss here the structure of outer layers of a $15M_\odot$ helium model with Galactic and LMC metallicities.
Previously we pointed out in the discussion on the physics of radiation driven winds, that at the sonic point, opacity must increase with radius, or $d\kappa/dr > 0$ (section 2.1.2). The opacity tables (Fig: 2.1), show that this conditions is fulfilled only in the certain regions with respect to the temperature, in particular, in the vicinity of opacity bumps. Thus, we expect the sonic point of our models to be located in these regions.
This is indeed the case. Figure 3.3, (top panel), shows, that for the high values of applied mass-loss rate, the flow accelerates in the hot part of the iron opacity bump, reaching the sound speed at $T_s \geq 10^{5.2}$. Such solutions with monotonic velocity profile we call **compact**. However, for a sufficiently small value of $\dot{M}$, a flow fails to reach the υ_s in the at the iron opacity bump, and after passing a peak, it decelerates. At the vicinity of the helium II opacity bump, the flow accelerates again, reaching the sound speed at $T \geq 10^{4.6}$. Such solutions we call **extended**. The value of the mass-loss rate below which the flow can no longer reach the υ_s at $T_s \geq 10^{5.2}$, is called the **critical mass-loss rate** $\dot{M}_{cr}$ (Grassitelli et al. 2018). More on the subsonic structure and the envelope inflation see in the Appendix B.
The bottom panel of Fig. 3.3, shows that the for a given value of mass-loss rate, the sonic point temperature depends on the metallicity, as the iron opacity bump becomes less prominent at lower metallicity (Fig: 2.1). Hence, the critical mass-loss rate depends on Z as well.
This is the motivation to include the metallicity uncertainty into our further work.

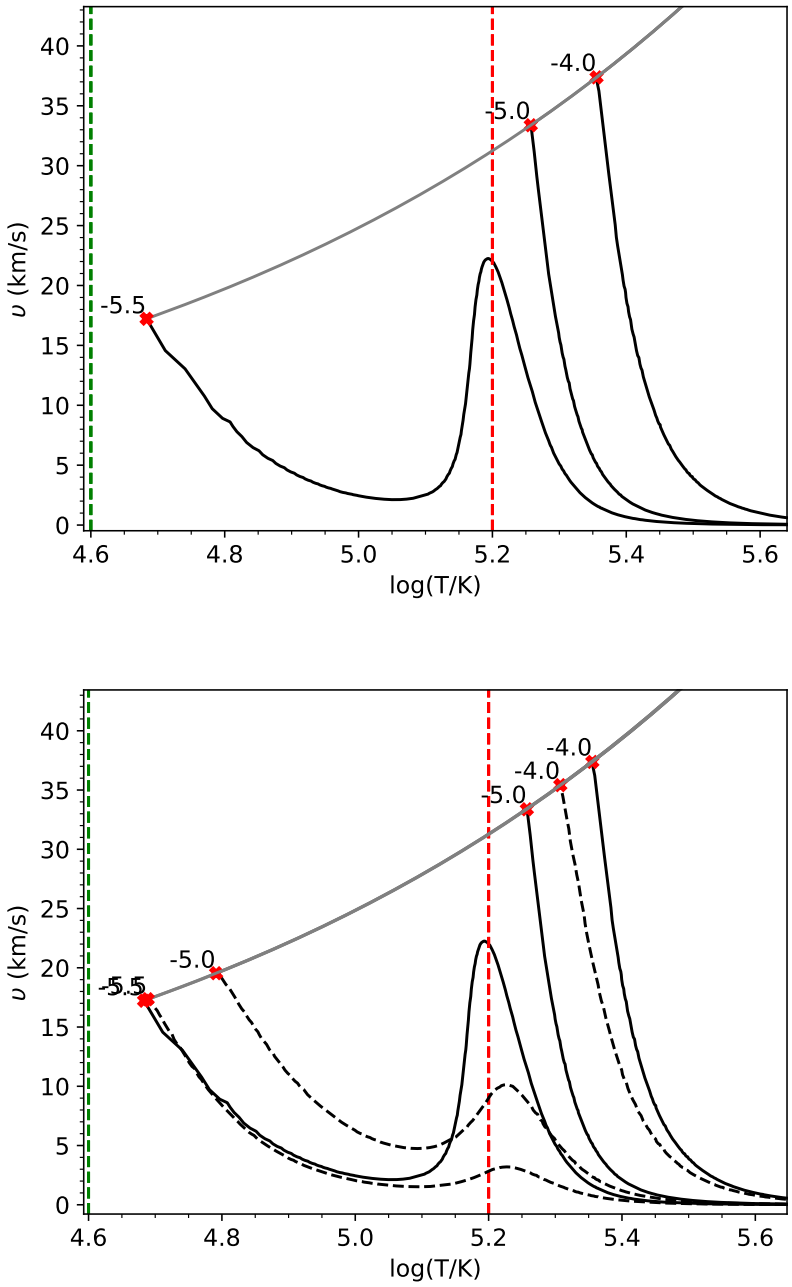

Figure 3.3.: Top panel: velocity profile with respect to the temperature of the $15M_{\odot}$ helium model with Galactic metallicity, with mass-loss rate in $\log(\dot{M}) \in \{-4.00, -5.00, -5.50\}$ indicated next to the end (sonic point) of the profile. Bottom panel: solid lines are the same velocity profiles as on the top panel, while the dashed profiles are for the $15M_{\odot}$ helium model with LMC metallicity. Vertical dashed red line corresponds to the peak temperature of the iron opacity bump $T_s \geq 10^{5.2}$

Chapter 4.

Results: Galactic WNE stars

In previous chapters we introduced the theoretical concepts this work is based upon. In particular, we described the an important tool for studying the WNE stars' physical properties, the Sonic Diagram, and WNE stars themselves in the Galaxy and LMC. We also discussed the structure of outer layers of helium models and pointed out, that depending on the applied mass-loss rate the subsonic structure may differ (see Appendix B).
In this chapter we discuss the results of our analysis of Galactic WNE stars and corresponding models, employing techniques and methods discussed in the previous chapter.

4.1. Modification of the Sonic Diagram

The sonic point temperatures T_s of Galactic WNE stars were investigated by Grassitelli et al. (2018). These authors showed that all WNE stars in the Galaxy have high sonic point temperatures ($\log(T) \geq 5.20$), consistent with winds launched to supersonic velocities by the momentum provided due to recombination of iron-group elements. In the above mentioned work, authors employed assumptions regarding the validity of the OPAL opacity tables and the adoption of a constant sonic point radius $R_s = 1R_\odot$. In this section we investigate effects of implementing a model-dependent R_s as a function of luminosity-to-mass ratio $\log(L/M)$ and sonic point temperature T_s.
The mass-luminosity relation for H-free helium models is provided by Langer (1989). However, this is relation for models at He-ZAMS. As a star evolves, burning helium into carbon and oxygen, the mean molecular weight in its interior increases, affecting the mass-to-light ratio of the star.
Large grid of H-free helium models with different initial masses and for various evolutionary stages allows to construct relations between the stellar luminosity, stellar mass (or $\log(L/M)$) and evolutionary stage.
Figure 4.1 allows to evaluate the L/M for a given L assuming the evolutionary stage. This, in turn, gives an evolutionary error bar for L/M of a given star. The right panel shows how sonic point radius depends on the L/M and T_s. Implemented in the figure 2.2 (right panel), the result is displayed in Fig. 4.2 (right panel).
The careful treatment of the sonic radius by inclusion of the Fig. 4.1 (right panel) leads to a more narrow range of possible sonic point temperatures for Galactic WNE star from previous $\log(T_s) \in (5.45, 5.20)$, to $\log(T_s) \in (5.40, 5.20)$. This can be understood from the continuity equation:

$$\dot{M} = 4\pi r^2 \rho \upsilon \tag{4.1}$$

where ρ is the density, and where where $\dot{M} \sim r_s^2$. Thus, as sonic radius increases with $\log(L/M)$, the $\dot{M}$ increases more steeply compare to the constant sonic radius case.

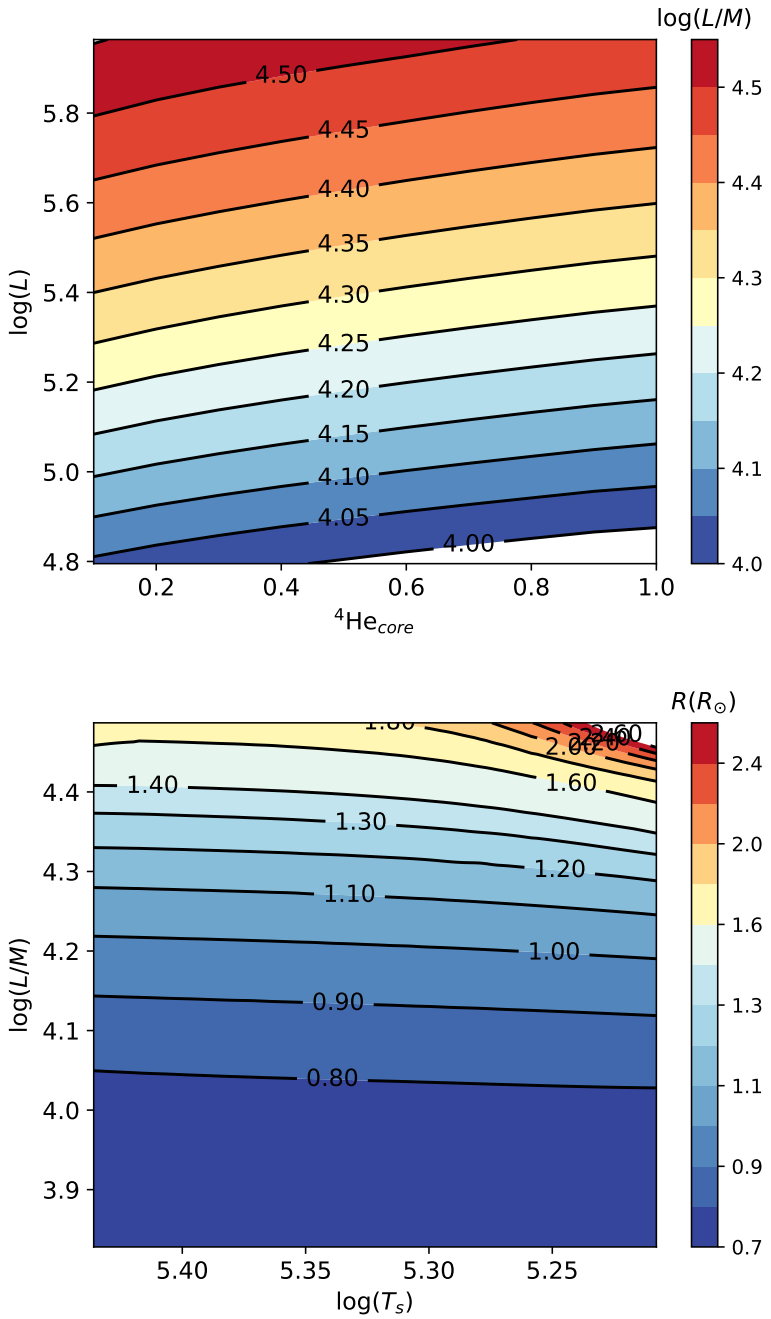

Figure 4.1.: Top panel: mass-luminosity relation in form of the relation between log L and log L/M as a function of the helium content in the core ${}^4He_{core}$. Bottom panel: the mass-radius relation in form of the relation between log L/M and $R(R_\odot)$ for a He-ZAMS models. Both panels are for the Galactic metallicity.

In particular, this change affects the position of the coolest WN4, that disappears from the right panel of the figure 4.2 due to its proximity to the peak of the Iron Opacity Bump. This proximity does not allow us to draw a definitive conclusion regarding this star subsonic structure, especially, if observational and evolutionary uncertainties, discussed below, are taken into account.

Fig. 4.2 also shows that high luminosity, and consequently L/M, of the star WR 123 requires ex-

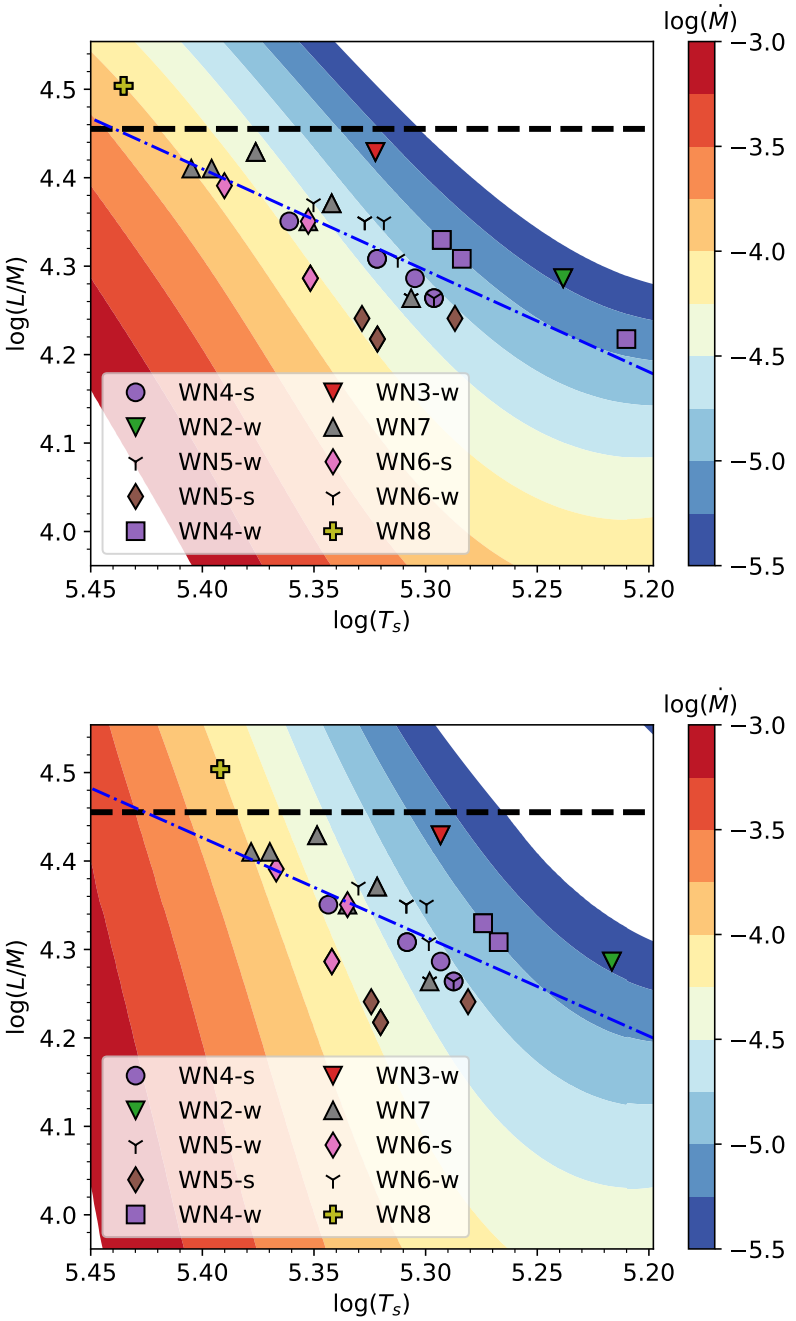

Figure 4.2.: Top panel: Sonic Diagram constructed with adoption of $R_s = 1R_\odot$, analogous to the Fig. 9 in Grassitelli et al. (2018). Bottom panel: Sonic Diagram, constructed with $R_s = f(\log(L/M), \log(T_s))$ from Fig. 4.1 (bottom panel). On both panels the H-free WNE stars are plotted based on their luminosity and mass-loss rate (Hamann et al. 2006), where the former was translated into the L/M, using the relation displayed in Fig. 4.1 (right panel) for He-ZAMS models. The horizontal black dashed line corresponds to the limit of the computed grid models and to the limit of OPAL tables. The blue line is a best fit.

trapolation techniques to be displayed on Sonic Diagram. The use of such techniques is justified by

the smooth and almost monotonic behavior of $\log(\dot{M})$ contours. While it might seem unnecessary to do that for one single star, the extrapolation would prove itself necessary for more stars, when the GAIA luminosities are considered.
The main conclusion here is that the model-dependent R_s does not change qualitatively the result regarding the wind acceleration mechanism. This confirms the previous findings by Grassitelli et al. (2018).

4.2. Uncertainties of observed WNE stars

In order to determine the luminosity of a star, the distance to it has to be known. For a single star, the distance determination is a complex procedure. However, if distance modulus is known, (from a cluster association, for example) the absolute visual magnitude, and luminosity can be inferred. However, in case of absence of a cluster association, distance modulus follows from the adopted absolute visual magnitude and is calibrated based on star's subclass (Hamann et al. 2006). This leads to a considerable degree of uncertainty.
Following Gräfener et al. (2017) and private discussion with the author, we adopt values of $\log L \pm 0.2$ for Galactic WNE stars.
In contrast to the luminosity, the mass-loss rate can be directly inferred from the analysis of the spectra. However, due to the imperfection of the fitting, uncertainties exist for the mass-loss rates as well. We adopt $\log \dot{M} = \pm 0.15$ for the Galaxy (Gräfener et al. 2017).
The commonly used value for the Galactic metallicity ($Z = 0.02$) is only an average value. Non-uniform metallicity distribution in the Galactic Disk is found by the Pedicelli et al. (2009) from the analysis of a large sample of Cepheids, where it is also argued that the metallicity is higher than average in the inner disk. However, no clear trend from innermost to outermost Galactic region was found. The paper concludes with an argument in favor of occurrence of chemical inhomogeneities across all Galactic quadrants. Moreover, Cepheid abundances indicate that these inhomogeneities are also present at smaller spatial scales.
The Galactic Bulge present itself with an increased average metallicity [Fe/H] = +0.06 with respect to the thin disk (McWilliam 2016). The metal-rich and metal-poor sub-populations with [Fe/H] = +0.3 and [Fe/H] = −0.3 respectively, represent limit cases. More recent work shows an even broader range of metallicities in the bulge: $-3.0 <$ [Fe/H] < -1.0 (Ness and Freeman 2016). In addition, recent high-resolution spectral analysis of evolved stars in young open clusters NGC 4609 and NGC 5316, with observed metallicities of [Fe/H] = $0.16 \pm +0.08$ and [Fe/H] = -0.02 ± 0.05 also indicate a large spread in the Galactic metallicity (Drazdauskas et al. 2016).
Recently, a set of helium star models with optically thick winds has been constructed and used to study the properties of the Galactic Wolf-Rayet stars, adopting metallicities $Z = Z_\odot$ and $Z = 2Z_\odot$ (Nakauchi and Saio 2018).
In light of aforementioned arguments, the metallicity [Fe/H] = +0.3, or equivalently $Z = 2Z_\odot = 0.04$ can be considered as an upper limit, while for the lower limit the metallicity of Large Magellanic Cloud, $Z = 0.008$ we will adopt as a first order approximation.
In addition, in present analysis we also include the uncertainty on the evolutionary stage of observed WNE. During the WNE phase there is a steady decrease in luminosity and in sonic radius (which occurs in response to the growing core of inert carbon). Due to the persistent loss of mass, however, the change in L/M is small. To estimate the evolutionary uncertainty, we assume a constant luminosity (an observed one) and based on that we obtained a range of possible L/M. The result is an error bar error on L/M, that represent how L/M of a star would change if it had different evolutionary stage, with the lowest value of L/M corresponding to He-ZAMS.
Together, the considered uncertainties on the luminosity and mas-loss rate, metallicity and evolutionary stage are shown in the figure 4.3. The meaning behind the gray crosses centered at the

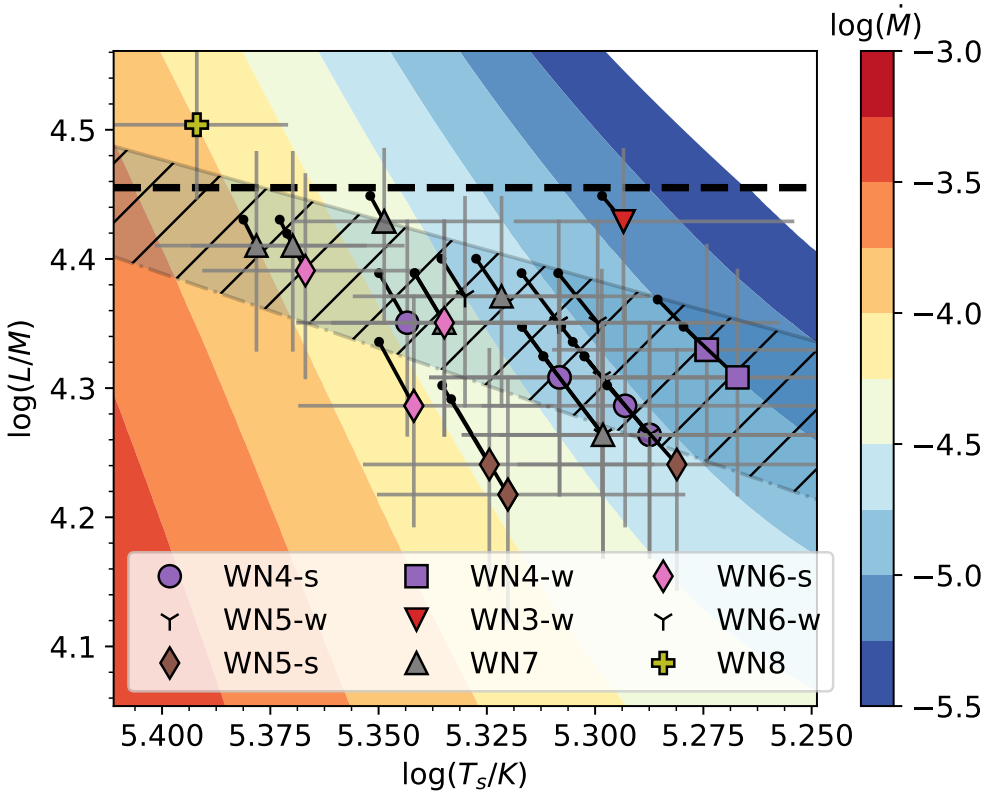

Figure 4.3.: Sonic Diagram constructed with adoption of a model-dependent sonic radius. The colored symbols are the H-free WNE stars from Hamann et al. (2006). Gray lines crossing at star's position are the observational uncertainties. Black lines emerging from stars are the uncertainty on the evolutionary stage. The crosshatched area shows best fit with metallicity uncertainty, which is limited by the the solid line on top, corresponding to the best fit of the observed Galactic WNE stars if $Z = 0.008$ metallicity is assumed, and the lower lying dotted-dashed black line for the super-galactic metallicity $Z = 0.04$. The thin dashed line in between is the best fit for the average Galactic metallicity. Thick black horizontal line limits the available parameter space, above which the extrapolation was used.

stars' position is the uncertainty for $(\dot{M}, L)$ translated into the plane $(T_s, L/M)$. Despite the fact that for the analysis of WNE stars from Hamann et al. (2006) we assumed the same uncertainties for L and $\dot{M}$, the size of crosses in the Sonic Diagram depends on stars' position, as contours of the constant mass-loss rate behaves non-linearly in the vicinity of the IOB. Thus, naturally, these uncertainties are larger for stars that lie close to the peak of IOB, at $\log T \approx 5.2$.
The best fit to observations is described by the equation:

$$\log(L/M) = 0.492 - 0.907 \log(T_s), \tag{4.2}$$

where the sign − indicates a declining slope.
The unknown evolutionary stage of observed WNE stars implies that the L/M can be higher than the mass-luminosity relation for He-ZAMS models predict. This possible increase in L/M is indicated with black lines (top panel) and colored lines (bottom panel) and it is immediately seen

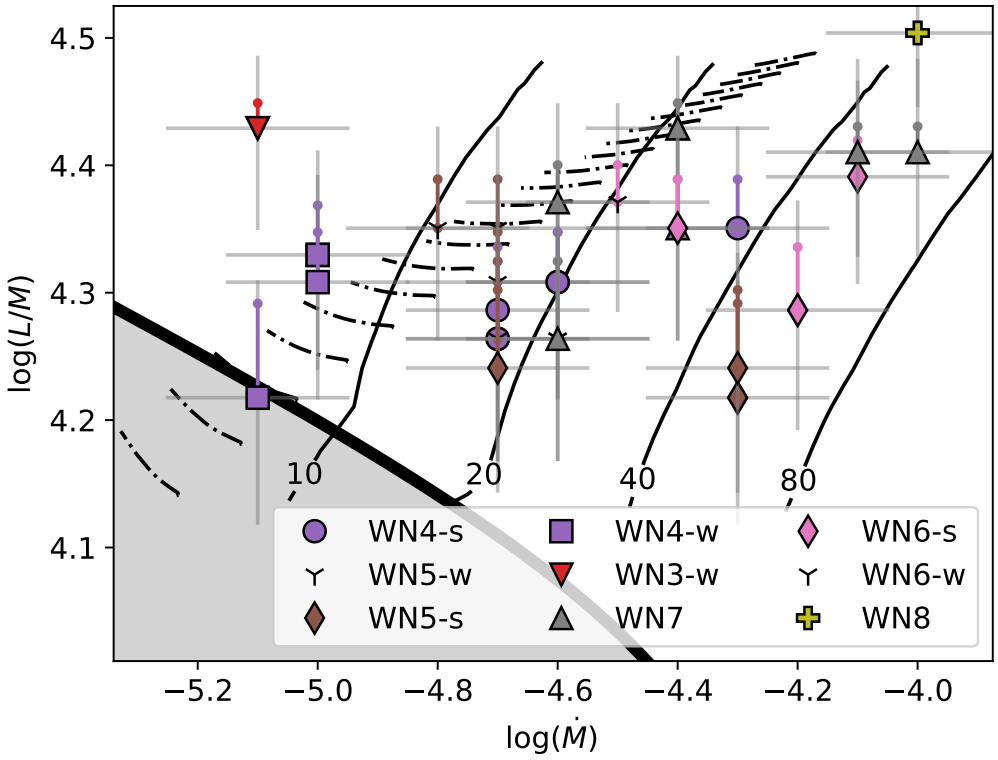

Figure 4.4.: $\dot{M} - L/M$ plot with Galactic WNE stars. Here, gray lines originating from stars' position show the evolutionary uncertainty. Black dashed-dotted lines are the evolutionary tracks of helium stars with initial masses from $9M_{\odot}$ to $30M_{\odot}$ with Yoon mass-loss rate prescriptions (Yoon 2017). The solid black line with a gray region below it is the minimum (critical) mass loss rate. Vertical solid black curves with numbers at the bottom, are the counters of constant optical depth τ, estimated from wind models computed with v_{∞} = 1800km/s and β = 1.

that in comparison to the observational uncertainties, the effect is small. In the figure 4.3 and 4.4 the evolutionary error bar appears smaller for more luminous stars. However, this is the result of our model analysis that shows, that such luminous stars undergo change in their surface chemical composition relatively soon after He-ZAMS, ceasing to be WNE. Ultimately, the most luminous WN8 star is beyond the parameter space and thus we provide no evolutionary error bar for it.

The evolutionary tracks for $(9 - 11)M_{\odot}$, in general, do not overlap with observations, except the narrow region around $L/M \approx 4.3$ and $\dot{M} \approx -4.8$. This might indicate that the adopted mass loss prescription is not very accurate in reproducing the $\dot{M}$ of Galactic WNE stars.

The evolutionary tracks for $(9 - 11)M_{\odot}$ lie below the critical mass-loss rates, implying that these models are extended (see Appendix B for more discussion), and considering the luminosities from Hamann et al. (2006), there are no corresponding observed WNE stars as was earlier pointed out by Grassitelli et al. (2018).

Analysis of the optical depth (see black contour lines in the figure 4.4) suggests that most of the WNE have an optically thick winds with $\tau > 10$. However, very early WN3 and some WN4, in particular WR 129, WR 51 and WR 44 have a low optical depth, $\tau < 10$. It might imply that

these stars have a partially optically thick winds. In contrast, late type WN6 and WN7 show higher optical depth. There appears to be a trend present, that τ increases with the WN subtype. The apparent exception is the most luminous and coincidently the latest WN8. This, however, as we shall present later, might be caused by the method used for the initial luminosity estimation, when we investigate GAIA luminosities.
To conclude this section, we state that present analysis confirms that the overwhelming majority of Galactic WNE stars have compact subsonic structure and winds launched by the increase in opacity at temperature $\approx 10^5$K. Sonic point temperatures of Galactic WNE stars closely follow the deduced from observations (empirical) sonic point temperature – luminosity relation. The inclusion of uncertainties into the analysis shows that the present degree of scattering can be explained by the unknown evolutionary stages of these stars, exact metallicity, as well as large observational uncertainties on the luminosity and mass-loss rate. The latter factor dominates for Galactic WNE. The optical depth at the sonic point seems to be increasing with subclass. The aforementioned results point toward a conclusion that the hydrostatic properties of Galactic WNE stars are mostly defined by one parameter, stellar luminosity, which was expected from theoretical arguments.

4.3. Photospheric Analysis

The result of the analysis of the Galactic WNE stars is shown in the figure 4.5.
The top panel (Fig. 4.5), the $T_s - T_{eff}$ diagram shows a remarkably linear relation between these two quantities with only one star, the WN3 (WR 46) being the outlier. It also shows that there appears to be a segregation between subclasses with the respect to the ratio T_s/T_{eff}, which approaches 1 for early type WN2 and rises for late-types, reaching maximum for WN8.
The slope of the empirical best fit to the observables is defined by the equation:

$$\log(T_{eff}) = 18.816 - 2.652 \log(T_s). \tag{4.3}$$

The HR diagram (Fig. 4.5, bottom panel) does not show a clear correlation between the stellar luminocity and the effective temperature, similarly, as there was no clear relation between the T_* and L (2.3). In HRD stars are distributed, according to their subclass with the early WN2 & WN3 being the hottest and the latest WN8 – the coolest, confirming that the temperature at the photosphere affects the line ratios, and thus, defines the subclass.
The main conclusion from this analysis is that we observe a linear relation between the sonic point and photospheric conditions of the Galactic WNE stars with early type WN having lower T_s and high T_{eff}, and vice versa for the late types.

4.4. Uncertainty on the Clumping Factor

Inhomogeneities in the wind of Wolf-Rayet stars complicate a definitive estimation of empirical mass-loss rates. Usually, these inhomogeneities are accounted for in a first-order approximation by introducing a clumping parameter D, which accounts for a higher density in the clumps, compare to the non-clumped medium in a given fraction of the total volume. For the Galactic WNE stars the $D = 4$ was initially adopted (Hamann et al. 2006). However, there have been arguments in favor of winds being more clumped and thus having $D \approx 10$ (Gräfener et al. 2017). Following the Yoon (2017), we rescale the empirical mass-loss rates to $D = 10$.
Result of the rescaling is shown in the figure 4.6, where it is seen, that the rescaling decreases the empirical mass-loss rates by $\Delta \log \dot{M} = -0.2$, which brings some of the stars, in particular the WR2 and WR129 below the critical curve. By doing so, it reduces the optical depth (see the

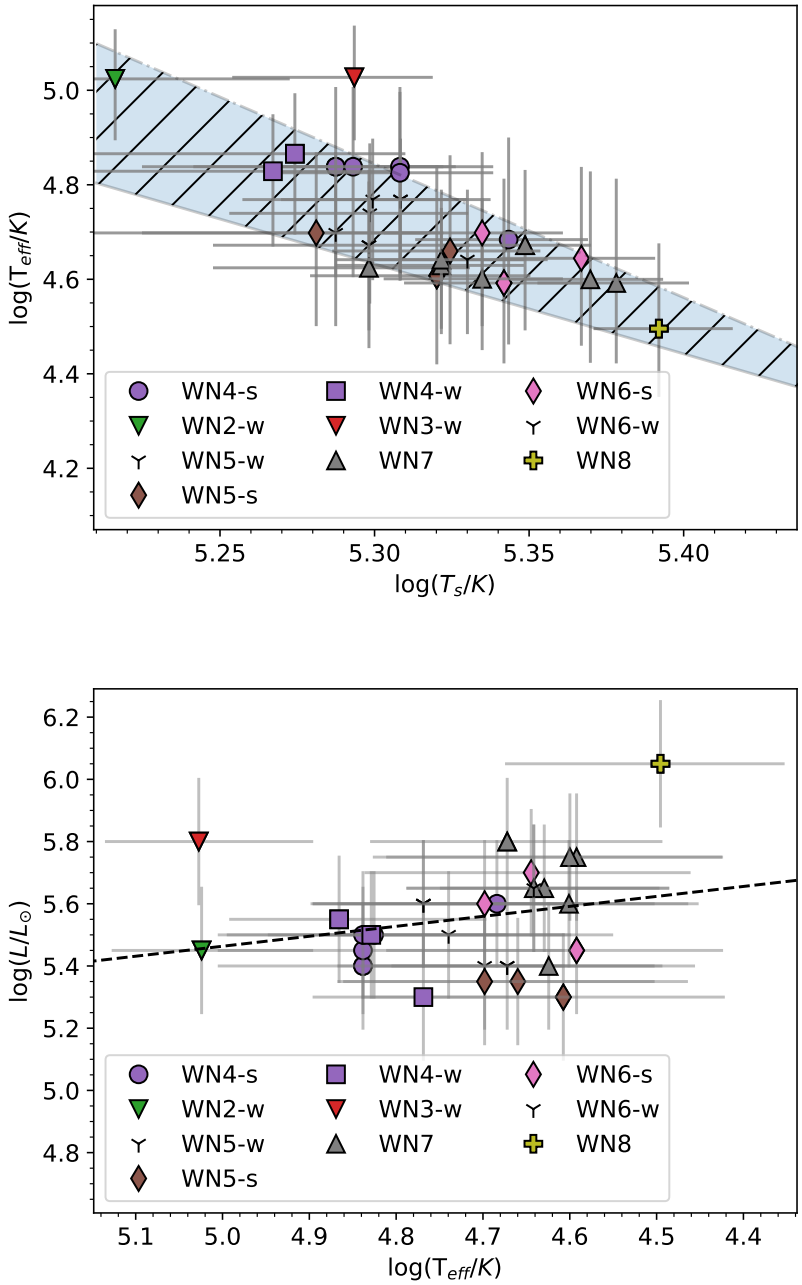

Figure 4.5.: Top panel: the $T_s - T_{eff}$ diagram, where the gray lines are the observational uncertainties. The blue dashed line is a best fit, while the crosshatched area around it is the uncertainty on the T_s, deduced from the metallicity spread. Bottom panel: the HR diagram, where on the x-axis the effective temperature at $\tau = 2/3$ (the photospheric temperature) is plotted. Black dashed line is a best fit. Thin gray lines are the observational errors in both panels. (See section 2.2 for the discussion on the origin on error bars on T_{eff})

contours of constant τ) of all the stars. the previously noted discrepancy between the evolutionary models and observed stars remains, as the rescaling of clumping factor simply parallel transports

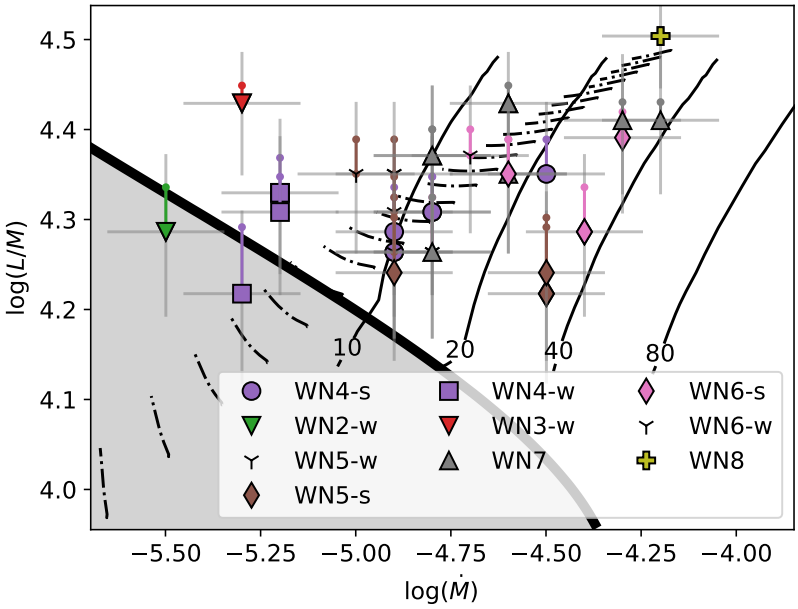

Figure 4.6.: $\dot{M} - L/M$ plot, where the empirical mass-loss rates were rescaled to clumping $D = 10$ Gray lines stretching from the stars position are the observational error bars. Colored lines with the dot on top are the evolutionary uncertainties. Black dashed-dotted lines are the evolutionary tracks. Solid black lines with numbers on the bottom, are the contours of constant optical depth τ, computed for the $\beta = 1.0$ $v_\infty = 1800$km/s wind parameters.

them.
Overall we conclude that rescaling to $D = 10$ is a useful exercise in a strive to account for all the uncertainties in the observed parameters of Galactic WNE stars. However, more convincing theoretical or observational arguments in favor of $D = 10$, or, better – an understanding of the properties and effects of wind inhomogeneities of the Wolf-Rayet stars are required. In the further investigation we will employ a $D = 4$.

4.5. The Epoch of GAIA

GAIA is a survey mission launched in 2002 with an aim to measure the position, distances and velocities of more than a billion stars in the Galaxy with an unprecedentedly high precision (Castelvecchi 2018). Besides its contribution to numerous branches of astrophysics that is hard to overestimate, it has allowed for the direct luminosity estimation of Galactic Wolf-Rayet stars, and for most of them, – for the first time since their detection.
The data on the parallaxes of the WNE stars is provided at the website `https://www.cosmos.esa.int/web/gaia/dr2`, and is discussed in Brown et al. (2018). The results of its conversion into luminosities is provided by Daniel Pauli and Dr. Grafener (personal communication). We, however, note, that the mass-loss rate and the photospheric conditions of WNE stars have not been changed in our analysis.
The change that GAIA data introduces is shown in the figure 4.7. The top panel shows the relative change in luminosity with regards to the original data from Hamann et al. (2006). Stars that

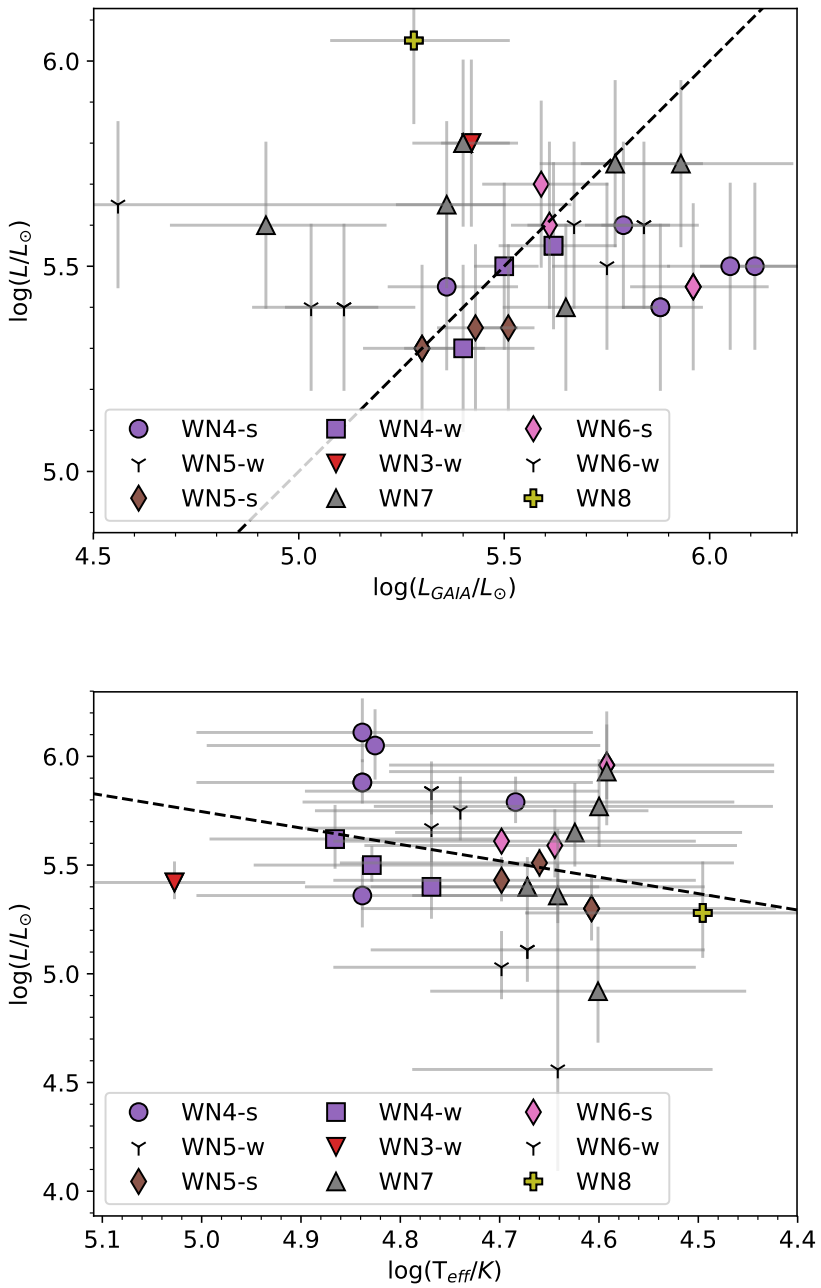

Figure 4.7.: Top panel: $L - L_{GAIA}$ plot, where the empirical luminosities are compared between Hamann et al. (2006) luminosities on y-axis and GAIA luminosities on x-axis. The black dashed line is a $y = x$ line. Bottom panel: the HR diagram, where the x-axis is the effective temperature at $\tau = 2/3$ (the photospheric temperature, estimated as before). The black lines with dots on top – are the evolutionary uncertainties. The black dashed line is the best fit. Thin gray lines are the observational errors in both panels.

preserve their L follow the diagonal. However, most WNE star, exhibit a considerable shift. In particular, data suggests that WN4 stars in general become brighter, while some late-types WN7

and WN8 have undergo a decrease in luminosity, with the WN8 being the extreme case (previously this star was the brightest, see Fig. 2.3). This particular change might be attributed to the fact that the distance modulus to this star was inferred from its magnitude. In addition, there has been indication of that this star shows variability (Marchenko and Moffat 1998).
Similarly, a star WR120 has significantly decreases its luminosity, which can be attributed to its unconfirmed cluster membership (Lundstrom and Stenholm 1984). The star that is now located in the far left (Fig. 4.7, top panel) WR115, gains a very large uncertainty in the new data and in its present position lies below the critical curve in $\log \dot{M} - \log L/M$ plane. Thus, we exclude it from our following analysis.
The new location of Galactic WNE stars on the HR diagram is shown in the figure 4.7, bottom panel. We use the T_{eff} from the previous analysis assuming that it would not change with new luminosities, which might be an oversimplification (Sander et al. 2018). However, our analysis show that the distribution of subclasses from the earliest on the left, to the latest on the right is preserved as well. In addition, the previously present trend, that with a decreasing T_{eff} the L rises is no longer present. On the contrary, the early type WN4 appears on average as bright as late type WN7. From our mass-luminosity relation (Fig. 4.1) we estimate that the lowest mass star is now WR120 with $M \approx 8M_{\odot}$ while the most massive is WR18 with $M = 38M_{\odot}$. Thus, our previous understanding that more massive, more luminous WNE stars should have more extended wind structures and thus lower photospheric temperatures seems not in full agreement with these new luminosity estimate.

Sonic point analysis the Galactic WNE stars with the GAIA luminosities suggests that **on average** early-type WN3 & WN4 have almost the same T_s, as late types WN7 & WN8. Same can be seen in figure 4.9. The previously noted trend of the sonic point temperatures following the empirical linear relation ($T_s - L/M$) is generally preserved with, however, different relation:

$$\log(L/M) = -5.966 + 1.938 \log(T_s), \tag{4.4}$$

and with WR123 (WN8) and the least luminous WR120 (WN7) being outliers, having much higher $\dot{M}$ that the empirical fit suggests.

The photospheric analysis is shown in figure 4.9. As that the distribution of WNE stars with respect to T_s becomes less homogeneous, spanning the range between $\log(T_s) \in (5.225, 5.400)$, it shatters the previous conclusion that there appears to be a linear relation in the $T_s - T_{eff}$ plane.
The use of more sophisticated statistical analysis, such as Spearman's rank correlation coefficient, is not practical owing to the large undersecretaries on T_{eff} and T_s.
Overall, the implications of the GAIA luminosities can be summarized as following. The sonic point conditions of the Galactic WNE stars still follow linear relation between the T_s and L/M, however less tight and with evolutionary uncertainties being of the same order as observational ones. The previously observed linear relation between the T_s and the T_{eff}, or equivalently, the subclass, is no longer present as early WN4 have $\log(T_s) \in (5.225, 5.350)$, while the late type WN7 show a similar range $\log(T_s) \in (5.250, 5.75)$ (in contrast to the figure 4.5, top panel). This implies that stars of various subclasses span across the similar L/M range, with the difference between them being the optical depth at the sonic point, that increases with the subclass.
The analysis of the wind models on top of compact subsonic stellar structure models and an attempt to reproduce the observed parameters, such as luminosity, mass-loss rate and terminal velocity of the Galactic WNE stars using the β-law is discussed in the Appendix E.

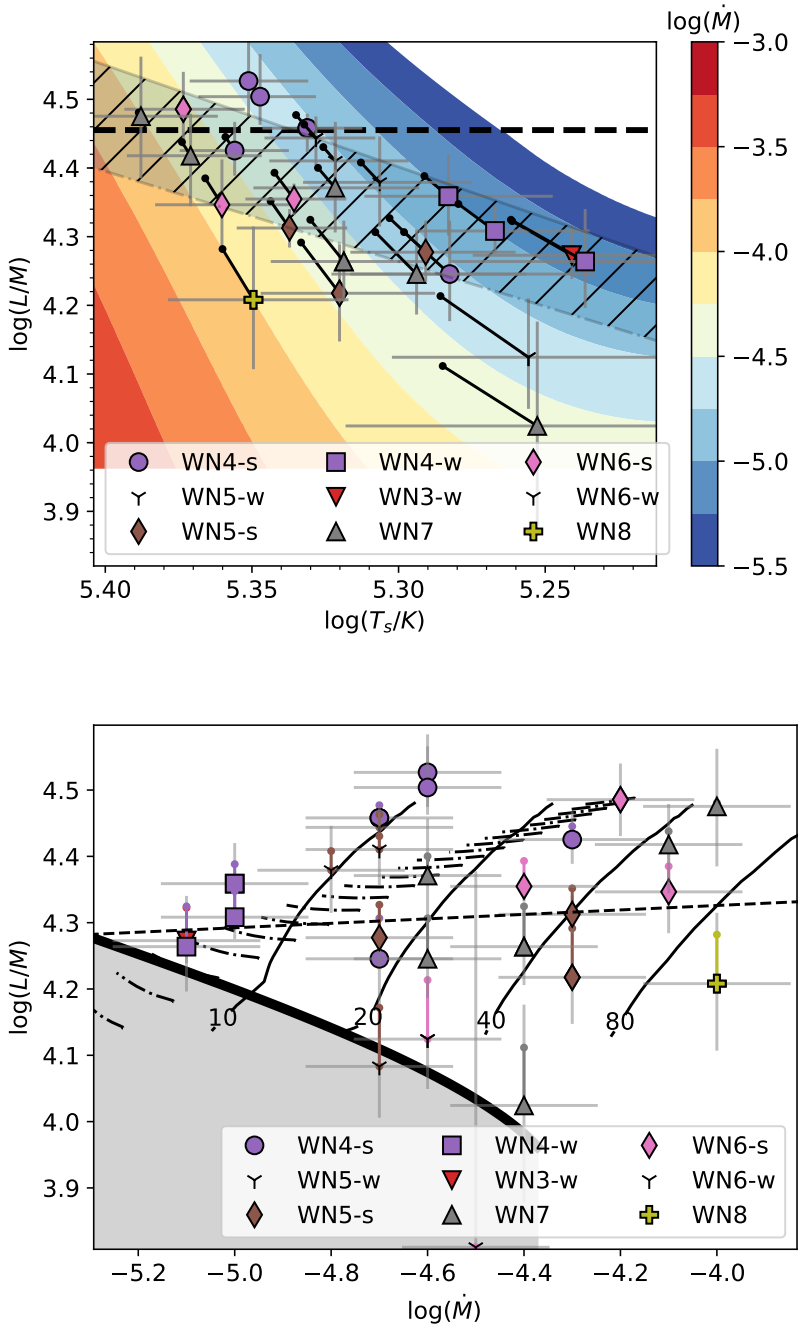

Figure 4.8.: Top panel: Sonic Diagram for the Galactic WNE stars with the GAIA luminosities. Bottom panel is a $\dot{M} - L/M$ plot with contours of constant optical depth τ. (For both panels detailed description see the Fig. 4.3 and Fig. 4.4

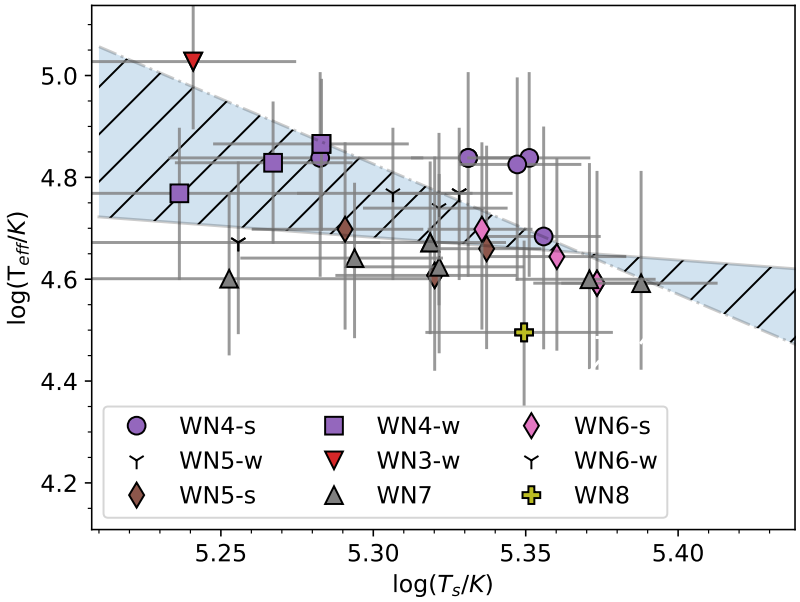

Figure 4.9.: The $T_s - T_{eff}$ diagram, where the gray lines are the observational uncertainties. The blue dashed line is a best fit, while the crosshatched area around it is the uncertainty caused by the unknown metallicity.

Chapter 5.

Results: WNE stars in Large Magellanic Cloud

In the previous chapter we discussed the properties of observed WNE stars in the Galaxy, employing the analysis based upon the already analyzed physical conditions at the base of the wind (Grassitelli et al. 2018). As these conditions has been noted to depend on metallicity (Vink and de Koter 2005, Petrovic et al. 2006) we first examine the sonic point conditions of our H-free helium models with LMC metallicity.

5.1. Models with LMC metallicity

$\log(\dot{M})$	$\log(L)$	$\log(\kappa)$	$\log(T_{eff})$	$\log(T_s)$	R_s	Γ_s	λ_s	HP	τ_s	$\log(T_{ph})$
-4.00	5.12	-0.01	5.07	5.26	0.88	0.998	7.41	8.36	112	4.70
-4.50	5.13	-0.06	5.07	4.89	0.89	0.885	7.79	7.45	34	4.47
-5.00	5.14	-0.04	5.07	4.78	0.89	0.933	8.21	7.39	11	4.48
-5.50	5.14	-0.02	5.07	4.68	0.89	0.968	8.64	7.39	3	4.54
-4.00	5.68	-0.25	5.12	5.32	1.32	1.020	8.03	9.00	60	4.83
-4.50	5.68	-0.26	5.12	5.27	1.33	1.010	8.52	9.25	17	4.91
-5.00	5.68	-0.27	5.12	4.79	1.37	0.985	8.82	7.75	5	4.57
-5.50	5.68	-0.26	5.12	4.68	1.37	1.000	9.26	7.76	1	4.61
-5.90	5.69	-0.26	5.12	4.61	1.38	0.994	9.62	7.78	1	4.61
-4.00	5.96	-0.35	5.14	5.35	1.67	1.016	8.35	9.32	41	4.90
-4.50	5.96	-0.36	5.14	5.30	1.69	1.007	8.85	9.65	12	4.99
-5.00	5.96	-0.37	5.13	5.25	1.74	1.004	9.36	9.99	4	5.08
-5.50	5.96	-0.37	5.12	5.19	1.89	0.999	9.90	10.33	1	5.16
-5.90	5.96	-0.37	5.10	4.58	2.01	0.996	10.05	8.15	1	4.58

Table 5.1.: Physical parameters of the $10M_\odot$, $20M_\odot$, $30M_\odot$ models (from top to bottom) for different values of mass-loss rate $\dot{M}$. The listed quantities are, starting from the left: mass-loss rate applied, luminosity, Rosseland opacity, effective temperature at the sonic point, temperature at the sonic point, sonic point radius, Eddington factor, photon mean free path, pressure scale height, optical depth, and temperature at the protosphere (where the $\tau = 2/3$). Wind structure is computed adopting $\beta = 1$ and $v_\infty = 1600$ universally.

As an example we summarize the main physical parameters at the sonic point for three stellar mass models with various applied mass-loss rates in the table 5.1, from which the following can be concluded:

- Higher critical mass-loss rate. The decreased prominence of the iron opacity bump at lower metallicity leads to the increase in critical mass-loss rate. This implies that at lower metallicity, higher mass-loss rates are required for the subsonic structure to be compact.
- Compactness does not imply high optical depth. Our low mass models show optically thick winds while being extended, and to the contrary, the most massive $30M_{\odot}$ model displays that compactness is not necessary accompanies an optically thick wind within our framework of assumptions regarding wind parameters.
- Departure from $\Gamma_s = 1$. In contrast to models with Galactic metallicity, models with LMC metallicity, especially low mass ones, show a decrease in $\Gamma = L/L_{edd}$ up to 0.9 at the sonic point. This implies that based that in Eq. 2.8 the opacity is now smaller than the Eddington opacity. Acknowledging this, however, we assume $\Gamma = 1$ for the further analysis, as most models still show $\Gamma_s \approx 1$.
- Departure from LTE. (The physical parameters of the radiation field of helium models with LMC metallicity are discussed below).

$\log(\dot{M})$	u	P_g/P_{total}	λ/c	t
-3.50	38.46	0.08	0.00	33
-4.00	36.20	0.04	0.00	17
-4.50	33.91	0.02	0.01	10
-5.00	19.54	0.23	0.02	0.5
-5.50	17.33	0.18	0.06	0.2
-5.90	15.72	0.14	0.14	0.1

Table 5.2.: Additional parameter list for the $20M_{\odot}$ model, that are related to the properties of the radiation field at the sonic point. The listed quantities are, starting from the left: mass-loss rate applied, velocity, ratio of gass pressure to the total pressure, ratio between the mean free path and the speed of light, optical depth parameter (Eq. 5.1).

In is important to note that the equation of stellar structure and evolution, used for the subsonic structure computations assume LTE ab initio. However, there are several indirect methods to estimate the proximity to the LTE, which are discussed in the Appendix B of Grassitelli et al. (2018). Following these authors we employ similar methods to analyze the radiation field of the representative $20M_{\odot}$ model. The main physical properties for such analysis are summarized in table 5.2.
Analysis of the anisotropy of the radiation field (Mihalas 1978) at the sonic point shows, that for the compact solutions, the departure from anisotropy is present but not large. However, the extended solution show a considerable increase in radiation field anisotropy.
Comparison between the pressure scale hight (that can be used as a characteristic scale of the system), and photon mean free path λ allows to infer the photon thermalization timescale. For the extended solutions, it is considerably large. Similar conclusion can be drawn by analyzing the λ_s/c, (where c is a speed of light), which is a radiation timescale associated with the photon thermalization. It is negligibly small for compact solutions, while rapidly increasing for the extended ones.
Additionally, the optical depth parameter t_s (Eq. 5.1) allows to infer the relative importance of the Doppler effects on the opacity (Nugis and Lamers 2002b),

$$t_s = \kappa v_{th} \rho \frac{dr}{dv} \tag{5.1}$$

where $v_{th} = \sqrt{\frac{2k_B T}{\mu m_H}}$ is a thermal, and all the quantities are taken at a sonic point.
If the t-parameter is smaller than 1, the velocity gradient is large at the sonic point and the Doppler effects and progressive line-deshadowing might be important for launching winds. Large values if ∇u and $t_s < 1$, found in extended solutions indicate that this might be the case.

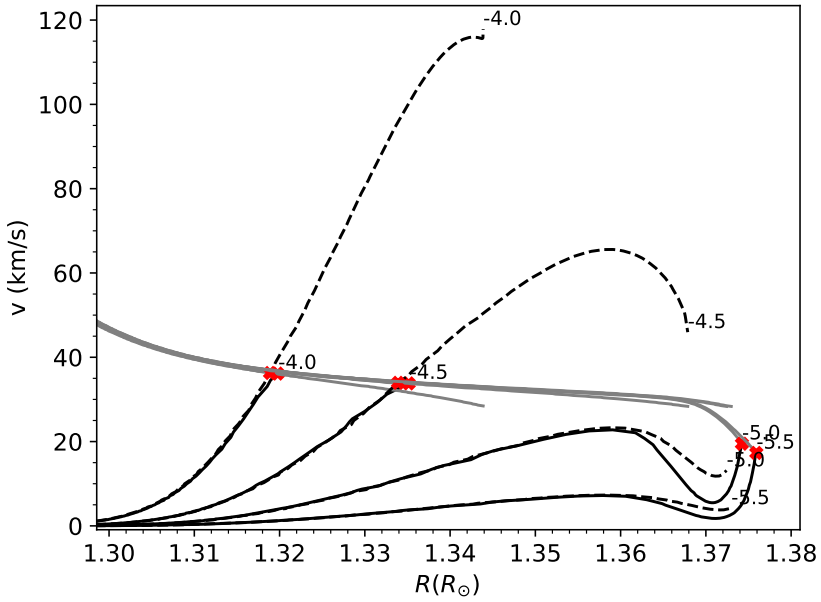

Figure 5.1.: Velocity profile of a $20M_\odot$ helium model with different applied mass loss rate in $\log(\dot{M})$ shown as labels at the end of corresponding profiles. Solid lines are the sonic point boundary condition models, while dahsed lines are plane-parallel gray atmosphere ones.

The similarity between the sonic point boundary condition models and plane-parallel gray atmosphere ones in terms of the subsonic structure is shown in the figure 5.1. For the compact solutions it is seen especially well. However, for the extended there is a difference, appearing in the outer most shells, which is caused by the fact that the extended plane-parallel gray atmosphere models do not reach sonic velocity prior to achieving the $\tau = 2/3$.
Overall, our models with LMC metallicity suggest that while compact solutions do have a radiation field at the sonic point close to the LTE, the extended ones deviate from it considerably. Acknowledging this, however, we will employ the same analysis method for the LMC WNE stars as for the Galactic WNE stars.

5.2. WNE stars in LMC

Using the models described above, we analyze the properties of the WNE stars in LMC, observational data for which was obtained from Hainich et al. (2015) and preliminary discussed section 2.2, figures 2.4 and 2.5.
In the Galactic case, all WNE stars seem to have winds launched to transonic velocities by the momentum provided by increase in opacity associated to the M-shell recombination of iron-group elements, and thus, they have a compact subsonic structure. In contrast, analysis of WNE in LMC

(Fig. 5.2) suggest that only the most luminous WN4 can be understood in the same manner. Most of the WN4 lie close to the critical mass-loss rate curve, the best fit for which is:

$$\log L/M = -31.789 - 26.175x - 7.200x^2 - 0.889x^3 - 0.041x^4 \tag{5.2}$$

where $x = \log \dot{M}$.

Low luminosity WN2 and WN3 lie below the critical curve and presumably have winds launched to the supersonic velocities by the partial recombination of helium. The robustness of this statement, however, slightly fades in light of the considered metallicity uncertainties in the LMC.

In a recent photometric study, an analysis of RGB stars in LMC was performed and averaged metallicity was estimated to be [Fe/H] = -0.37 ± 0.12 dex (Choudhury et al. 2016). However, study of spectra of an old population of RR Lyrae stars [1] (Haschke et al. 2012) suggested a rather broader range of observed iron content: [Fe/H] = -1.50 ± 0.24 dex. Considering these observations we set $Z = 0.01$ as a highest limit and $Z = 0.004$ as a conservative lower limit. We note, however, that a $Z = 0.006$ would be a better choice in light of aforementioned studies.

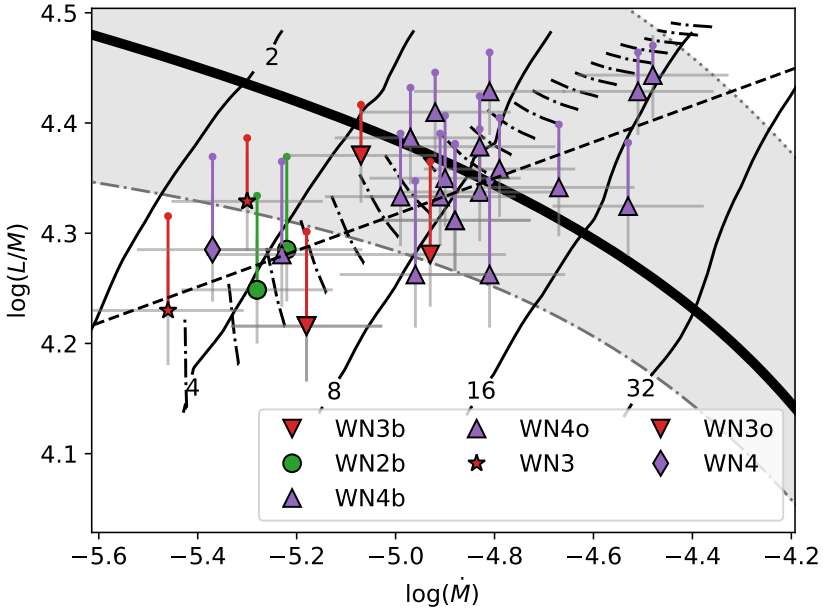

Figure 5.2.: Mass loss is a function of a luminosity-to-mass ratio. Colored symbols are the observed H-free WNE stars in LMC (Hainich et al. 2014). The colored vertical lines originating in the stars' position are the evolutionary error bars. Gray crosses at stars' position are the observational error bars. A thick black curve is a critical mass-loss rates for the IOB driven winds (Computed assuming $Z = 0.008$). The gray area around it is the metallicity uncertainty on it. The diagonal solid black lines with numbers on them are the contours of constant optical depth (Computed with $v_\infty = 1600$, $\beta = 1$). Black dashed-dotted lines are the evolutionary tracks of the $10M_\odot - 30M_\odot$ models. The black dashed line is a best fit for plotted WNE stars.

Metallicty uncertainty analysis (see gray region in the Fig. 5.2), indicates that for most of the WN4 the mechanism that the wind launching mechanism depends strongly on adopted value of

[1] RR Lyrae stars are the pulsating horizontal branch aging stars of spectral class A or F, with a mass of around half the Sun's

Z. In the region with high metallicity, it is presumably IOB, while HOB prefers lower metallicity. Less ambiguous, however, the situation for less luminous early type WN2 & WN3. Regardless of adopted value of Z, these stars seems to have an extended subsonic structure with winds launched at HOB.
Analysis of an optical depth (see diagonal contour lines in the Fig. 5.2) suggests that overall, τ in LMC stars is lower than corresponding τ in the Galaxy, which was expected considering the lower metallicity, and thus, opacity. However, we note once again, that our τ estimation is accurate to the order of magnitude and serve as an crude indicator. Having said that, we note that the most luminous WN4 have the highest τ, that is indicative of an optically thick wind. In contrast, the early-type WN2 & WN3 have $\tau < 10$. This might imply that these stars have only partially optically thick winds with photosphere located close to the sonic point.
Evolutionary tracks of H-free helium models (see short dot-dashed lines in the Fig. 5.2) show overall a better agreement between observations and theoretical prescription for the mass-loss rate, than in the Galactic case (Fig. 4.8, bottom panel). It also appears that with lower observational uncertainties on the luminosity and mass-loss rate and, the evolutionary uncertainty becomes dominant in constraining stars' L/M.
Interestingly, the critical mass-loss rate curve passes through the WNE population and through evolutionary tracks. This implies, that there are stars that during their evolution should cross it. In other words, stars with initial mass $M \sim 18 M_{\odot}$ during their WNE phase undergo a change in their subsonic structure from extended to compact. The exact mechanism how this is being realized in nature is currently being investigated. Possible intermediate configurations exhibiting multiple sonic points and ejection of mass, contained in the extended layers are studied. However, we note that the mass of the corresponding shells of our models is of order $10^{-10} M_{\odot}$.
Now, assuming that the WNE population in LMC is divided into the compact, (In BAT99 catalogue these are: WR7, WR17, WR24, WR26, WR65, WR88, WR94, WN131, WN13) and extended (WR1, WR2, WR3, WR5, WR15, WR23, WR37, WR41, WR46, WR48, WR51, WR56, WR57, WR75, WR86, WR124, WR128, WR134), we investigate their sonic point conditions separately. The result is shown in the figure 5.3.

Compact. The top panel (Fig. 5.3) show that the compact WN4 have a rather narrow spread in sonic point temperatures, i.e. $T_s \in (5.20, 5.30)$, which is comparable to the spread in T_s of the low luminosity Galactic WN4, while most of the luminous Galactic WN4 have no counterpart in LMC (Fig. 4.8, top panel). This is because, while in both cases WN4 span across similar range of $\log(\dot{M}) \in (-4.5, -5.0)$, the GAIA luminosities for WN4 are considerably larger. Notably, the original observational data from Hamann et al. (2006), show a better agreement between WN4 population in the Galaxy and LMC (Fig. 4.3).
Overall, if the observational and evolutionary uncertainties are considered, the sonic point conditions of the compact WN4 stars in LMC mostly depend on one parameter, stellar luminosity with the best fit being,

$$\log(L/M) = 0.489 + 0.744 \log(\dot{M}). \tag{5.3}$$

However, the metallicity uncertainty on the best fit (in particular, the lower limit), leads to the absence of stars with compact subsonic structure (see Fig. 5.2).

Extended. Considering the extended models (Fig. 5.3 bottom panel) we note again that these stars have much lower sonic point temperatures $\log(T_s) \in (4.85, 4.70)$, which corresponds to the hot part of the helium II opacity bump. The empirical best fit for these stars is:

$$\log(L/M) = 1.607 + 0.560 \log(\dot{M}), \tag{5.4}$$

quite shallower than the best fit for the compact WN4.

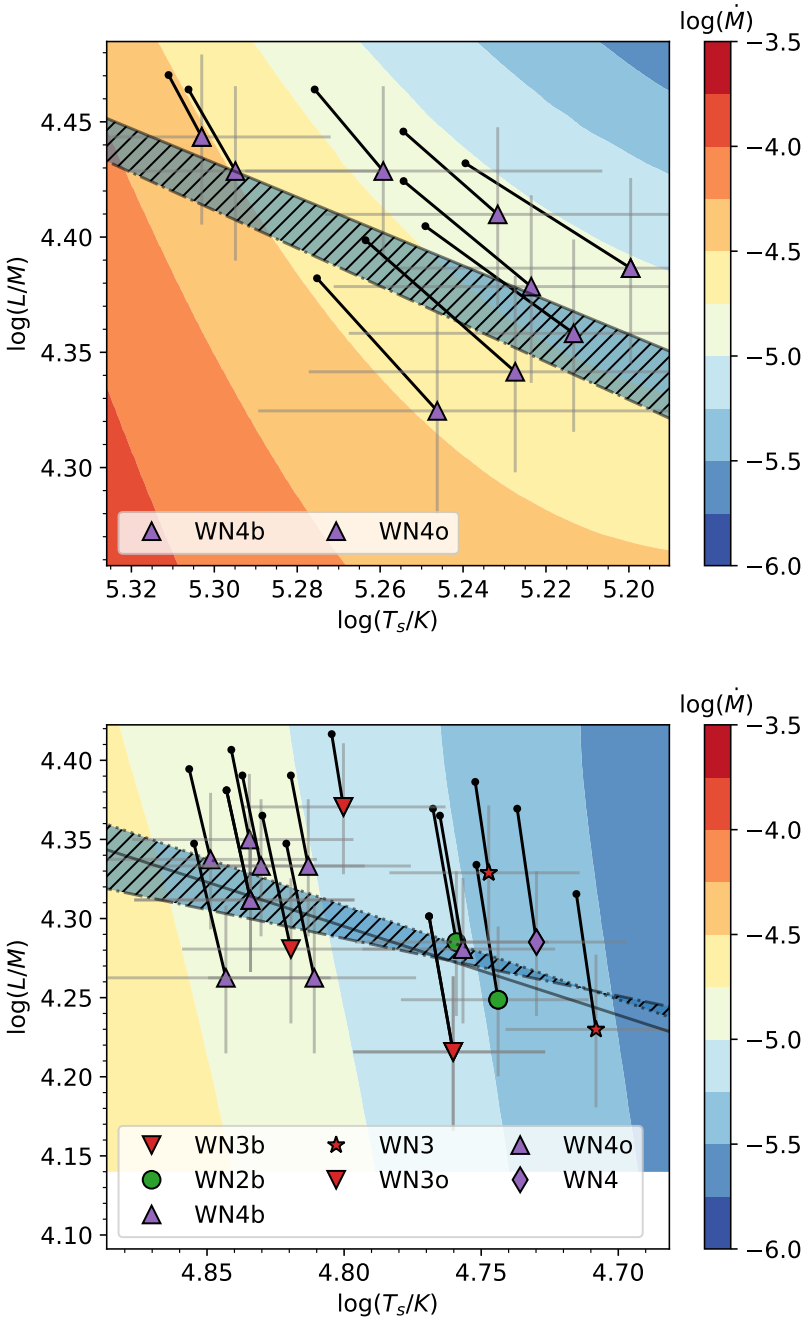

Figure 5.3.: Top and bottom panels are the Sonic Diagrams, for the hot part of the iron and helium II opacity bumps respectively for the LMC metallicity. WNE stars are plotted using their L and $\dot{M}$, obtained from (Hainich et al. 2014). (For legend description see the Fig. 4.3)

The total population seems to be clustered in two regions: hot region with $\log(T_s) > 4.80$ and dominated by WN4, and slightly cooler, with $\log(T_s) \leq 4.75$, dominated by the early-type WN2 & WN3. However, due to the considerable observational and evolutionary uncertainties the definitive conclusion cannot be drawn and only mentioned because author finds it quite peculiar how stars of the same spectroscopic subclass, namely, WN4, can be be both compact and extended with

drastically different sonic point conditions. **This can be reconciled if the highest boundary of our metallicity uncertainty, namely $Z = 0.01$, shown in the Fig. 5.2, is implemented.** In this case, mostly WN4 appear compact.
Overall, the main conclusion of sonic point condition analysis of WNE stars in LMC is the following. Our models with metallicity $Z = 0.008$ suggest that the most luminous WN4 are compact with IOB driven winds, while low luminosity WN2 WN3 and certain WN4 appears to be extended with HOB driven winds. The exact ratio between the two populations strongly depends on the metallicity. In particular, if $Z = 0.01$, all WN4 appears to be compact.
Inside of their respective domains (regarding the subsonic structure), and within all considered uncertainties, sonic point properties of H-free WNE stars mostly defined by the stellar luminosity, with the empirical relation being shallower for extended than for compact.

5.2.1. Photospheric Analysis

Photospheric conditions of compact WN4 (Fig. 5.4, top panel) are similar to the Galactic WN4 (Fig. 4.9), with $\log(T_{eff}) \approx 4.8$ (while, on average, lower sonic point temperatures). The relation between the T_s and T_{eff},

$$\log(T_{eff}) = 0.796 + 0.771 \log(T_s), \tag{5.5}$$

is quite flat and is being tightly followed by almost all WN4, except WR 88. However, large uncertainties on the T_{eff} mitigate this discrepancy. Notably, the extended WN4 alone, on the figure 5.4 (bottom panel), seem to have a similar slope. However, the presence of WN2 with a very high $T_{eff} \approx 5.0$ affects it so that an overall slope for the best empirical fit for extended WNE stars is:

$$\log(T_{eff}) = 6.594 + -0.360 \log(T_s). \tag{5.6}$$

Note, that in our work we assume that the WNE stars in LMC have optically thick winds. This implies that the photosphere lies in the supersonic part of the flow, or equivalently, that $T_{eff} < T_s$. However, our analysis (5.4, bottom panel) suggests that most of the extended WNE have $T_{eff} \geq T_s$. This is an apparent disagreement with aforementioned statement and requires an explanation. We suggest the following.

- Metallicity effects. From Fig. 5.2 it is seen that if the higher metallicity is assumed, most of the WN4 become compact with much higher T_s.
- Weaker assumptions. One of our assumptions laid in the basis for of this analysis is not applicable. For example, LTE at the sonic point is not a very strong assumption for the extended solutions. In addition, large velocity gradient at the sonic point of extended models, decreases the applicability of OPAL opacity tables.
- Importance of not considered factors. In this analysis we neglected magnetic fields and rotation which might modify the sonic point conditions.

The most extreme outliers are the earliest WN2, namely WR 2 and WR 5. For them, even if the considered uncertainties are taken into account, the T_{eff} is much higher than T_s, which implies that either these stars have a partially optically thin winds and photosphere is indeed located in the subsonic part of the flow, or that other factors affect the appearance of these stars, such as rotation and/or magnetic fields, not considered here.
With regards to the WR 2, there has been indications that this star has an unusually strong ionizing flux (Nazé et al. 2003) and spectra that required high T_* for the spectra fitting, thus placing this star

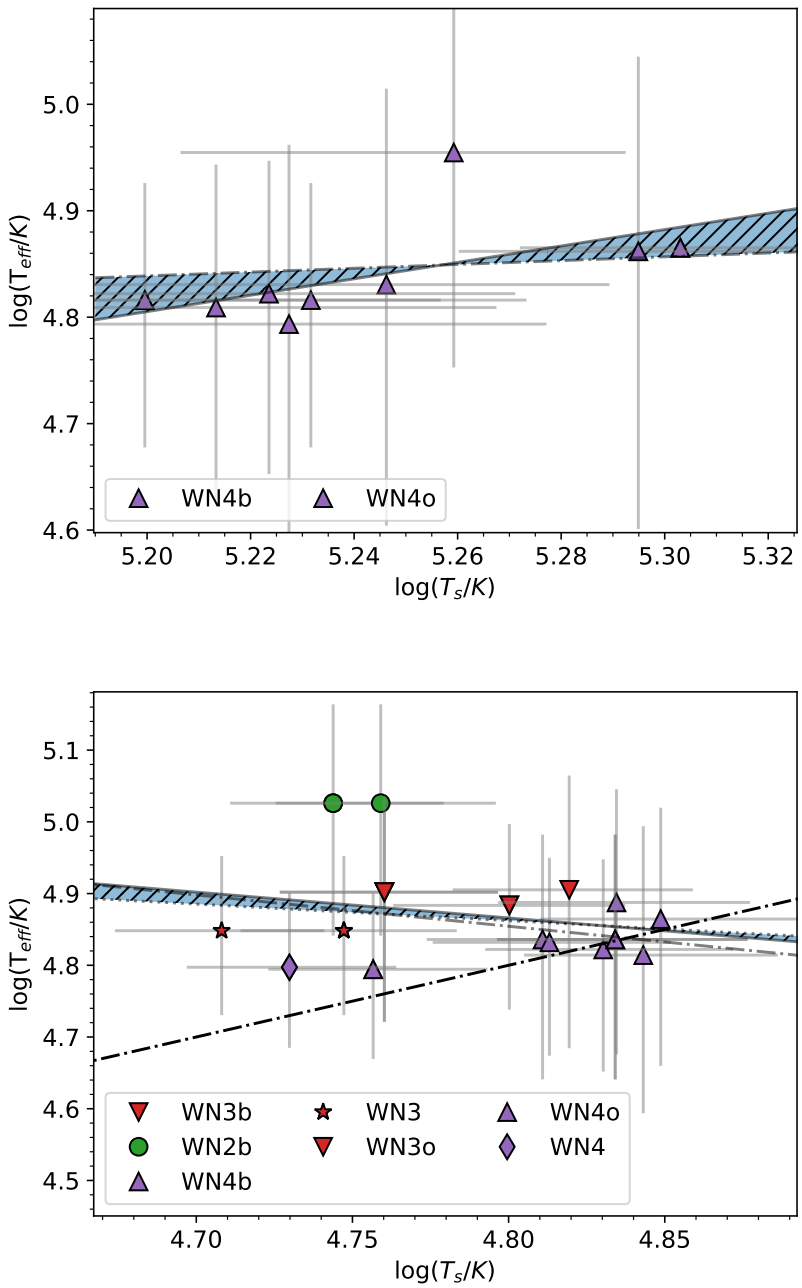

Figure 5.4.: Top and bottom panels are the $T_s - T_{eff}$ diagrams for the IOB (compact) and HeOB (extended) domains respectively for the LMC metallicity. T_{eff} for the WNE stars is computed using the T_* and transformed radii R_t from (Hainich et al. 2014). The dashed black line on the bottom panel is a $T_s = T_{eff}$. The gray region is $T_s < T_{eff}$. Blue crosshatched region is the best fit with metallicity uncertainty on T_s.

into the zone of parameter degeneracy (Hainich et al. 2014). Similarly, the WR 5, falls into the parameter degeneracy zone, having high T_* due to the included line-blanketing into the modeling (Hainich et al. 2014).

Overall, the main conclusion is the following. The photospheric conditions of the compact WN4

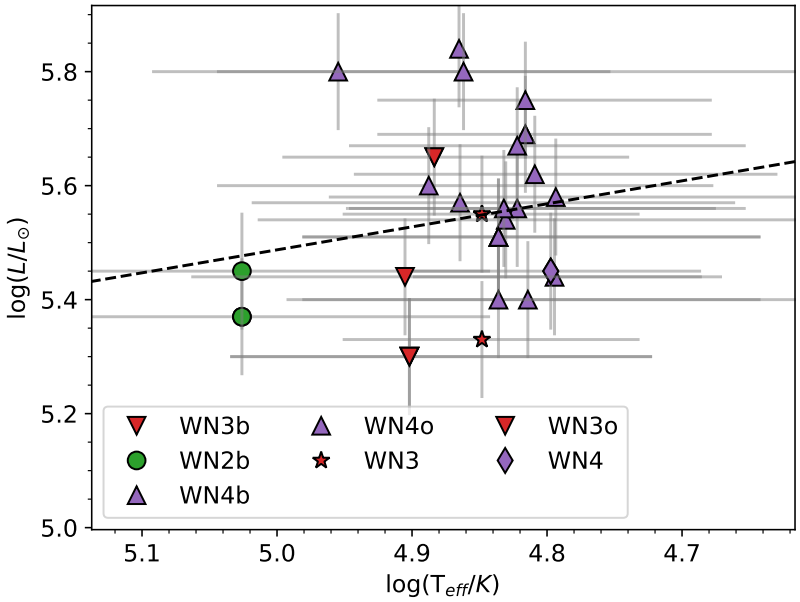

Figure 5.5.: HR diagram for the WNE stars in LMC.

are similar to the corresponding WN4 in the Galaxy, following a similar relation between the sonic point and photospheric temperatures. The extended WN4, while displaying similar photospheric temperatures, have much lower sonic point temperatures and complex subsonic structure. In addition, the requirements for all Wolf-Rayet stars to have an optically thick winds, imposes a limit on their minimum photospheric temperature. This constrain in case of helium opacity bump driven winds is not met by the earliest WN2. The nature of this discrepancy might lie in the rotation and magnetic effects not considered here or in the degeneracy in the initial estimation of the photospheric temperature.

The analysis of the wind models on top of compact subsonic stellar structure models and an attempt to reproduce the observed parameters, such as luminosity, mass-loss rate and terminal velocity of the LMC WNE stars using the β-law is discussed in the Appendix F.

Chapter 6.

Results and Conclusion

6.1. Results

6.2. Results

6.2.1. Galactic WNE stars

Our investigation shows, that the Galactic WNE stars have compact subsonic structure and winds launched by an increase in opacity at the iron opacity bump. This result is in agreement with previous work by Grassitelli et al. (2018).

We find, that stars follow a rather narrow linear relation in terms of T_s and L/M (Fig. 4.3). The sonic point conditions follow this relation within the considered uncertainties on evolutionary stage, metallicity, as well as observed luminosity and mass-loss rate. The optical depth at the sonic point is found to be increasing from early to late subclass (Fig. 4.4). The investigation of usually neglected evolutionary effects shows that during the WNE phase, the $\log(L/M)$ of our models changes by less then 0.1, which is in most cases smaller than the observational uncertainty from Hamann et al. (2006).

Modification of the clumping factor to $D = 10$ decreases the empirical mass-loss rates by $\Delta \log \dot{M} = -0.2$, making the aforementioned conclusion regarding the subsonic structure of some of the early-type WNE stars questionable (Fig. 4.6). Besides that, our results change only quantitatively, but not qualitatively.

The investigation also showed that there appears to be an inverse linear relation between the sonic point temperature and photospheric temperature, with the earliest WNE subclass having the lowest T_s and the highest T_{eff} (Fig. 4.5, top panel).

The relations between the T_s, and L/M, and T_{eff} (Fig. 4.3 and Fig. 4.5, top panel) suggest that the the photospheric properties of the Galactic WNE stars are mostly defined by stellar luminosity and the conditions at the base of the wind, which in turn depend on metallicity.

Considering the luminosities from GAIA DR2 (Brown et al. 2018) for the Galactic WNE stars, instead of Hamann et al. (2006) (with unchanged mass-loss rates and photospheric conditions), the aforementioned results become less clear. While, there is still an overall linear relation between the T_s and L/M present, (though with a different slope), the correlation is less narrow (Fig. 4.8 top panel). The inverse proportionality between the subclass (or T_{eff}) and T_s is much less apparent as well. Instead, various subclasses span across a similar range of T_s (Fig. 4.9).

Using the velocity gradient at the sonic point, computed with the sonic point boundary condition hydrodynamic models (Fig. E.1 bottom panel), we constrain the acceleration in the supersonic part of the flow, under the assumption of validity of the β-law. This analysis suggests that wind models with $\beta = 1.00 \pm 0.15$ are able to display terminal wind velocities in the observed range (Fig. E.2).

The lowest value of β is preferred by the latest subtypes, while the highest β is preferred by the earliest subclass.

6.2.2. LMC WNE stars

Models of H-free helium stars show that while the radiation field at the sonic point of compact solutions close to LTE, there is a departure from LTE for extended ones (Tbl. 5.2). This decreases the robustness of our results for the latter, because our assumptions concerning the validity of the diffusive approximation for radiative transfer and the validity of the adopted opacity tables start to drop.
Analysis of the subsonic structure of the LMC WNE stars with assumed metallicity $Z = 0.008$ suggests that the most luminous WN4 are compact. Their winds are driven by the momentum provided by increase in opacity in the hot part of the IOB, similar to the Galactic WNE stars (Fig. 5.2). Low luminosity WN2 WN3 and WN4, however, seem to have an extended subsonic structure with density inversion and low, ($\sim 10^4$K) sonic point temperatures corresponding to the hot part of the helium-II opacity bump. The location of the boundary between the compact and extended domains strongly depends on the metallicity.
The change in $\log(L/M)$ during the evolution in WNE phase of our models with $Z = 0.008$ is around 0.1 for low mass stars which in case of the LMC, is compatible or even larger than the observational uncertainty (Fig. 5.2).
Because of the presence of two domains with respect to the sonic point conditions, there are appears to be no single relation between the T_s, L/M and T_{eff}. Instead there are separate, but mostly linear relations between T_s and L/M in compact and extended domains, that observed WNE stars follow within the considered uncertainties (Fig. 5.3).
We find that the sonic point temperatures of the compact WNE stars seem to be almost independent from the photospheric ones within the considered uncertainties (Fig. 5.4 top panel). In the extended domain, the sonic point temperatures of WNE stars is of order of 10^4K, and thus close to the photospheric ones within considered uncertainties (Fig. 5.4, bottom panel). In addition, the two hottest (in terms of T_{eff}) WN2 appear to have $T_s < T_{eff}$, contradicting the initial assumption of the optically thick winds with photosphere lying in the supersonic part of the flow.
The analysis of the wind acceleration at the sonic point (with assumed validity of β-law) suggests that the compact WNE stars can be understood as having $\beta \approx 1$, similarly to the Galactic WNE stars (Fig. F.2). However, models with the extended subsonic structure show a much steeper velocity profile and larger values of outflow acceleration at the sonic point. Thus, the corresponding WNE stars might be understood as having steeper β-profiles with $\beta \approx 0.5$.

6.3. Conclusion and Discussion

We started this work by mentioning the disagreement between the observed variety of the WNE stars spectral subtypes (with different photospheric conditions for a given luminosity) and the theoretical perditions. Our results suggest that the conditions at the base of the WNE wind, mostly in terms of sonic point temperature and L/M, can explain the variety of observed photospheric conditions in the Galaxy. In fact, the correlation between the sonic point and photospheric temperatures indicates the crucial importance of the former for the wind properties determination.
However, in light of new observational data being available for the Galactic WNE stats from GAIA DR2, an additional investigation is required to confirm our results.
In addition, we find that the mechanism of wind acceleration to the transonic velocities of massive WNE stars is an increase in opacity in the vicinity of opacity bumps. The iron opacity bump is of key importance for launching winds in the Galactic WNE stars and most luminous LMC WNE

stars. In the most of the WNE population in the LMC, however, the helium-II opacity bump is responsible for accelerating outflows to transonic velocities.
Thus, further instigation with the focus on lower metallicity WN stars e.g. stars in the SMC and population III stars, would be beneficial for constructing a more comprehensive picture of wind launching mechanism and sonic point conditions.
In the LMC we found two populations of WNE stars: with compact and extended subsonic structures with winds launched by the increase in opacity in the vicinity of iron and helium-II opacity bumps respectively. Thus, the photospheric properties of all WNE stars in LMC cannot be explained by the luminosity and the base of the wind conditions only. This result suggests a necessity for further investigations of the sonic point conditions at the base of the wind at lower metallicity.
With regards to the analysis of uncertainties, we determine that in the Galaxy, the uncertainty on the parameters determined from observations, such as luminosity and mass-loss rate, are dominant over the unknown evolutionary stage. However, in the LMC, the metallicity and evolutionary uncertainties dominate.
Overall, our work contributes to the understanding of the structure of stars close to the Eddington limit and mechanism of acceleration of their strong, dense winds. This works highlights the importance of performing hydrodynamic stellar structure calculations (in contrast to the purely hydrostatic ones), the important influence that the wind has on both the quasi-hydrostatic and photospheric properties of stars, as well as the key role played by the metallicity and the iron bump in defining the structure and appearance of post main sequence massive stars.

Appendix A.

Super-solar Metallicity

Here we briefly discuss an additional grid of models computed for the analysis of Galactic WNE stars with the supersolar metallicity, $Z = 0.04$. Grid consists of models in the mass range $M \in (10, 16)M_{\odot}$, $\log(\dot{M}) \in (-3.5, -5.5)$ and evolved till the $^4He_{core} = 0.1$ or till the change in surface composition sets in.

Figure A.1 (Top panel) shows that the at higher metallicity, the WNE phase has shorter duration. At $Z = 0.02$ (Fig. 3.2) the change in the surface composition for $16M_{\odot}$ model starts at $^4He_{core} \approx 0.3$, while at $Z = 0.04$ it begins at $^4He_{core} \approx 0.5$. In addition, the steepness, in terms of $^4He_{core}$ per L/M, with which the surface compositions changes for $Z = 0.04$ is higher, meaning that while for Galactic metallicity, $10M_{\odot}$ model even at latest stage of evolution, where $^4He_{core} \approx 0.1$, the surface composition is unchanged, while the $10M_{\odot}$ model with $Z = 0.04$ at $^4He_{core} \approx 0.1$ does show changes at the surface.

Figure A.1 (bottom panel) shows that at higher metallicity the sonic radius for the same value of L/M is larger. This is caused by more metal rich models being more inflated. In more details the inflation, the inflation criteria, and the effect of metallicity on it, are discussed in the Appendix B.

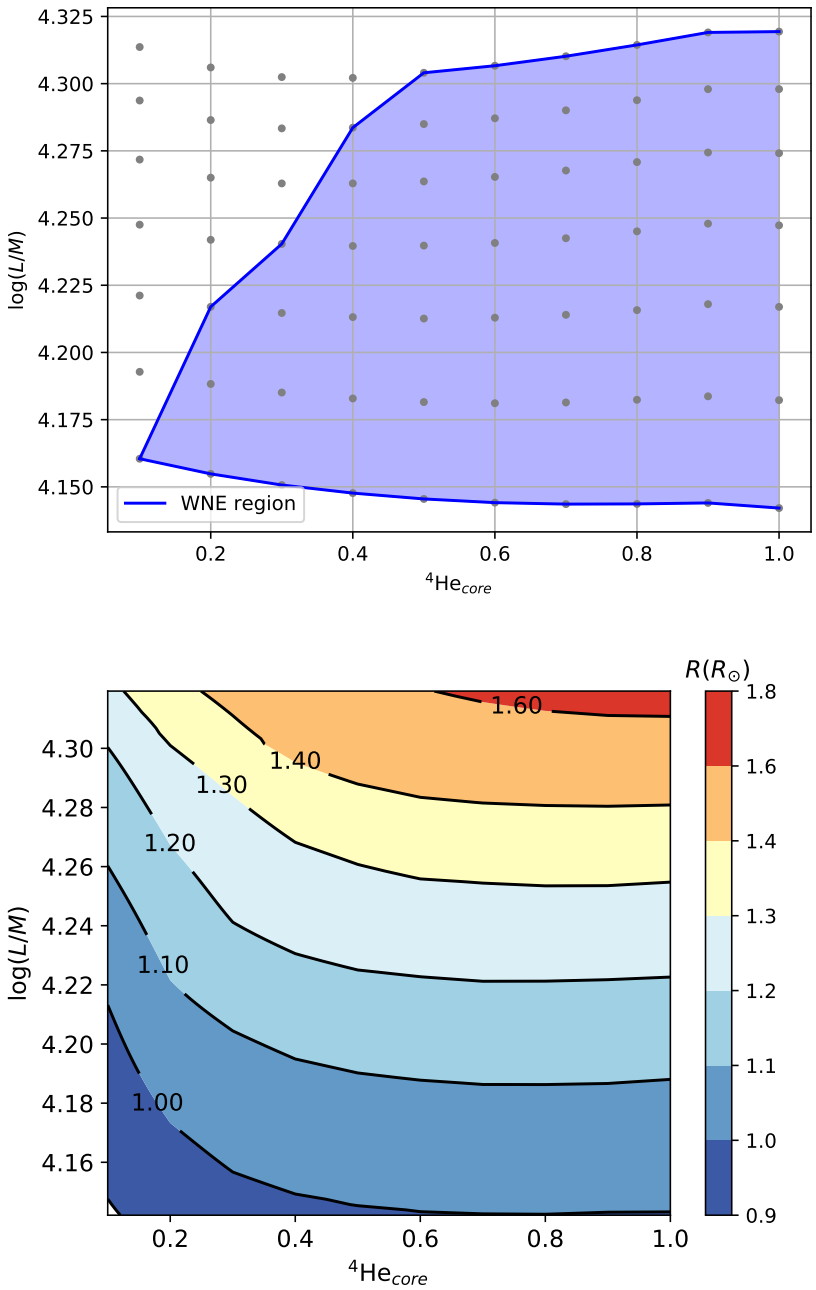

Figure A.1.: Top panel: mass-luminosity relation in form of the relation between $\log L$ and $\log L/M$ as a function of the helium content in the core ${}^4He_{core}$. Bottom panel: the mass-radius relation in form of the relation between $\log L/M$ and $R(R_\odot)$ for a ZAMS models. Both panels are for the $Z = 0.04$ metallicity.

Appendix B.

Subsonic structure and envelope inflation

Here we discuss the subsonic structure of helium models with focus on the inflation criteria.
The suggested criteria for the onset of inflation, (Grassitelli et al. 2018), the equation 1.8, has a solution shown in Fig. B.1. The solution can be understood as a point at which speed with which the density decreases, from rising switches to falling. This point is located deep within the outer layers, and models show that the location of this point appears to be independent from the applied mass-loss rate.
The position of the inflection point, R_{infl} does depend on L/M similarly to the R_s (Fig. B.2). However, for all considered models the dependence on the applied mass-loss rate is negligible, especially in the range of observed values of $\dot{M}$ in the Galaxy and LMC.
Change in metallicity affects the R_{infl} weakly as well, and the noticeable increase in inflection point radius is only visible for a low mass, low L/M models, where the R_{infl} is larger for a lower Z environments, while decreasing less with rising $\dot{M}$.

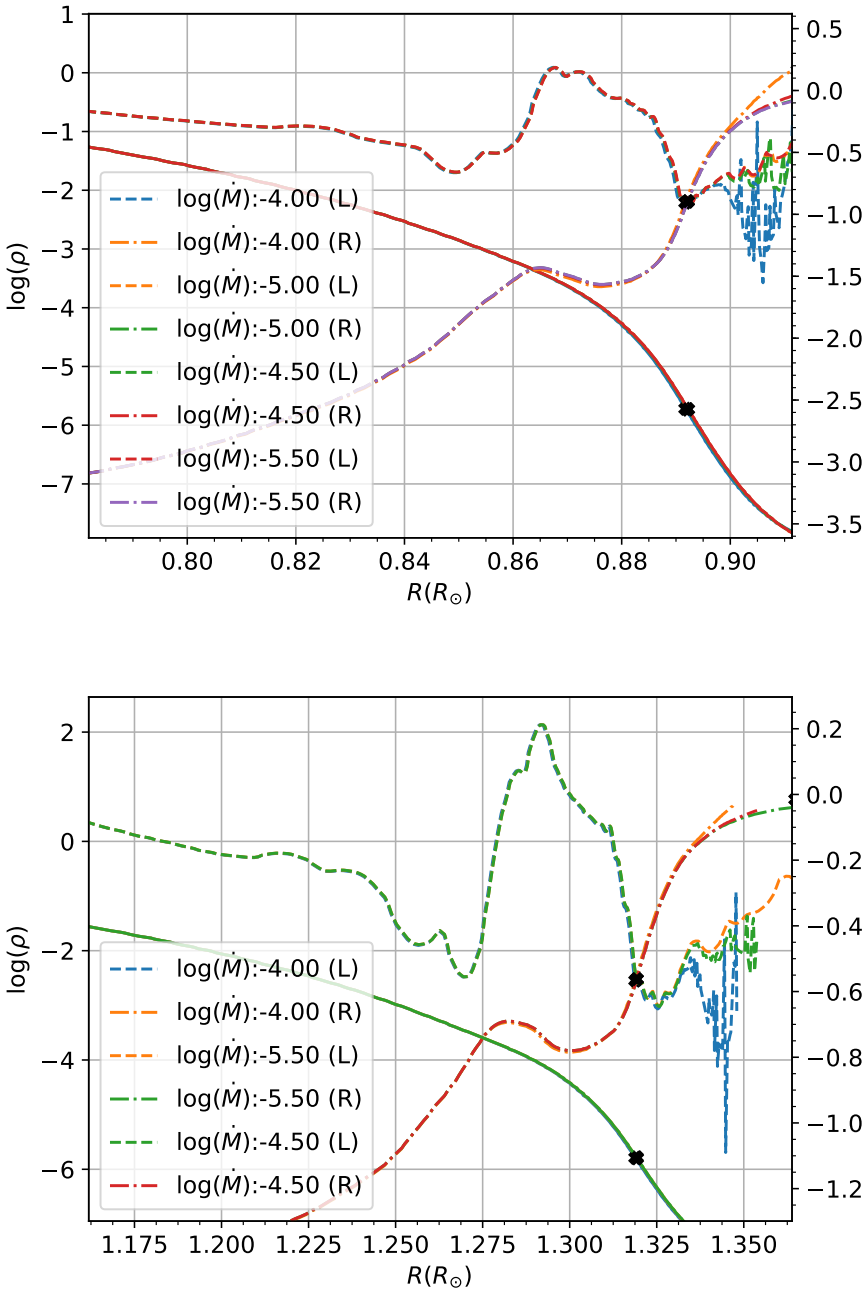

Figure B.1.: Density profiles (colored solid lines) for different values of $\log(\dot{M})$ for $10M_{\odot}$ model (top panel) and $20M_{\odot}$ model (bottom panel) with Galactic metallicity. The colored dashed lines represent the left-hand-side of the equation 1.8, while the colored dot-dashed lines represent the right-hand-side of this equation. The black points indicate the solution to the equation 1.8.

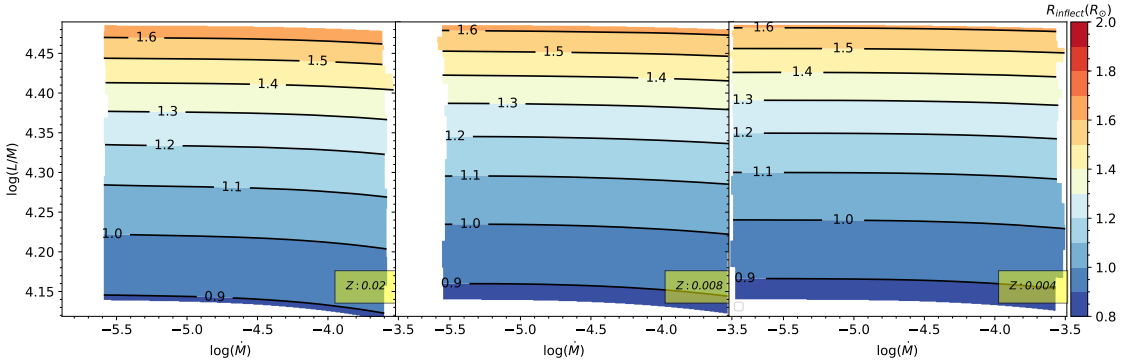

Figure B.2.: The location of the inflection point as a function of mass-loss rate and L/M for three grids of models: $Z = 0.02$, $Z = 0.008$, $Z = 0.004$ metallicity from right to left respectively. All models are at He-ZAMS.

Appendix C.

Numerical estimation of critical mass loss

In order to estimate the critical mass-loss rare, the procedure shown in the Fig. C.1 is performed for every stellar model. Obtained value of critical mass-loss rate is used to interpolate the R_{crit} and T_{crit}, using the interpolated univariate spline of 3rd order.
The method shown in the Fig. C.1 inherently takes into account the dependence of the sonic radii on the applied mass-loss rate and sonic point temperature, and thus it is model-dependent. However, based on the fact that $\Gamma_s \approx 1$, or equivalently, $\kappa_s \approx \kappa_{Edd}$, there is a model-independent way to estimate the critical mass-loss rate from the OPAL opacity tables, described in Grassitelli et al. (2018). However, as the Sonic Digram itself, this method relies on the assumed R_s for every L/M and thus might prove to be less accurate if the R_s steeply depends on the L/M.

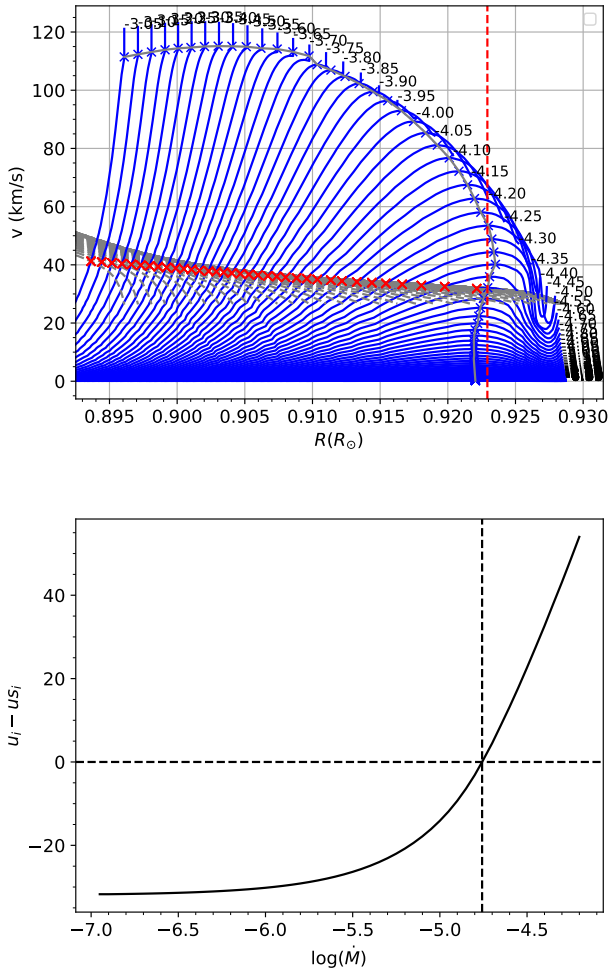

Figure C.1.: Top panel: set of velocity profiles for a range of applied $\log(\dot{M}) \in (-3.00, -6.50)$ with the step of 0.05 for the $10M_{\odot}$ model with Galactic metallicity. Blue crosses at the end of the velocity profiles indicate the maximum value of the velocity. Gray lines represent the sonic velocity profile for every $\log(\dot{M})$. The red crosses lying on them – are the sonic points of the corresponding velocity profiles. The solid gray line, passing trough extrema of velocity profiles is the interpolated curve, connecting them. The vertical dashed red line located at the critical radius R_{crit}. Bottom panel: on the x-axis is the $u_{max}[i] - c_s[i]$, or the difference between the maximum of the velocity profile and the value of the sonic velocity the same R for every velocity profile (for every $\log(\dot{M})$). The y-axis is a mass-loss rate $\log(\dot{M})$. The horizontal dashed line is the $u_{max}[i] - c_s[i] = 0$, where the velocity (at its maximum value) equals to the sound speed. The vertical dashed line is the interpolated value of mass-loss rate for that point, which is a critical mass-loss rate.

Appendix D.

Numerical estimation of the smooth transonic solution

The grid of models consisting of sub- and super-sonic parts allows to obtain the unique solution that smoothly passes through the sonic point. This is done via method shown in the figure D.1.
Similar approaches for the determination of the stellar model that posses a smooth transonic velocity profile have been considered by other groups: Gräfener et al. (2017) and Nakauchi and Saio (2018). However, in all of them parameters of the β-law, such as v_∞ and exponent β were set ab initio, based on the values obtained from observations of WNE stars. In this work we investigate a parameter space (v_∞, β) that would result in models that cover the parameter space in ($\log(\dot{M}), \log(L/M)$) of observed WNE stars.
It is however, important to note that the validity of the single β-law has been recently questioned by the Sander et al. (2015), where it was suggested that this might be an oversimplification, as the full hydrodynamic models show the plateau in the velocity field, that is not reproduced by the single $\beta-$law. .

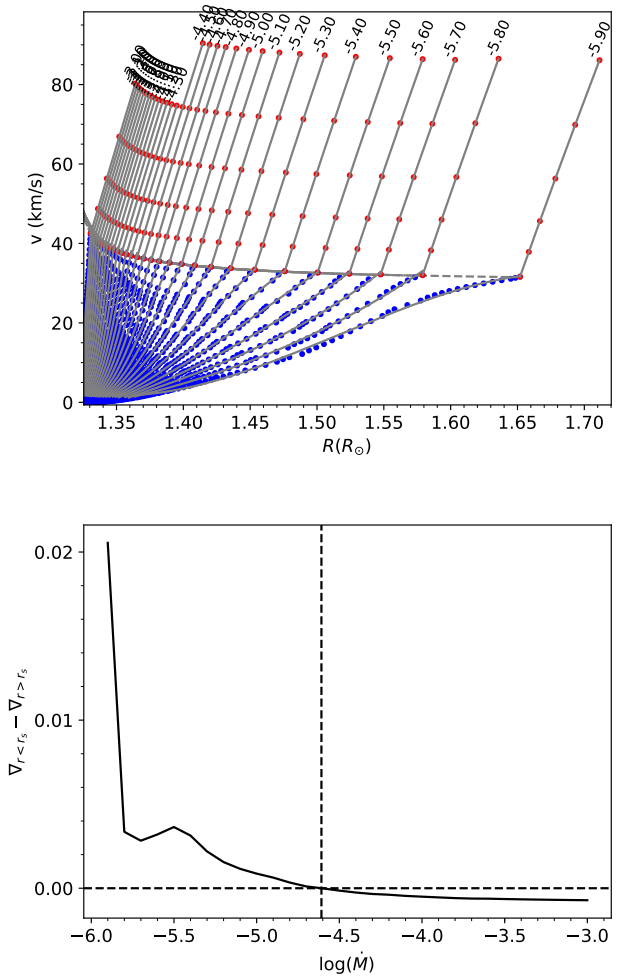

Figure D.1.: Top panel: set of velocity profiles in the sub- and super-sonic parts for a range of applied $\log(\dot{M}) \in (-3.00, -5.90)$ with the step of 0.1 for the $20M_{\odot}$ model with Galactic metallicity. Dark blue points are the velocity profile computed with BEC, and the gray curves passing though them are the Univariate spline of 3rd order, that is fitted by least square method. The red points display the $\beta-$profile. Gray lines crossing them are the Univariate spline of 3rd order fitted by the same method. The labels at the end of the profile is the applied value of $\log(\dot{M})$. Bottom panel: on the x-axis is the absolute value of $\nabla_{r<r_s} - \nabla_{r>r_s}$, (where $\nabla = du/dr$) or the difference between the velocity gradient at the end of the subsonic velocity profile and the beginning of the supersonic velocity profile (defined by the β-law). The y-axis is the mass-loss rate $\log(\dot{M})$. The horizontal dashed line is the $\nabla_{r<r_s} - \nabla_{r>r_s} = 0$, where the velocity gradients are equal. The vertical dashed line is the interpolated value of mass-loss rate for that point, which is a critical mass-loss rate.

Appendix E.

Note on the wind models with Galactic metallicity

In previous sections of this chapter we analyzed the observed properties of Galactic WNE stars. We discussed the empirical relations between the physical parameters, such as L/M, $\dot{M}$, $\log(T_s)$, and $\log(T_{eff})$, where the $\log(T_{eff})$ and probably τ appears to be the only definitive characteristic(s) for a given subclass. However, while the data from Hamann et al. (2006) show a clear correlation between the photospheric and sonic point temperatures (Fig.4.5), the GAIA data show an apparent absence of such relation.

In this section we introduce wind models on top of compact subsonic stellar structure models in a strive to reproduce the observed parameters, such as luminosity, mass-loss rate and terminal velocity of the Galactic WNE stars. The method is based on the assumption of validity of the single $\beta-$law (Eq. 2.7). The condition of the smoothness (differentiability) of the velocity profile at the sonic point implies that

$$\lim_{r\to r_s}\left(\frac{d\upsilon}{dr}\Big|_{r_s-0} - \frac{d\upsilon}{dr}\Big|_{r_s+0}\right) = 0. \tag{E.1}$$

Equation 2.7 describes the velocity profile for a given pair of wind parameters β, which is the exponent of the profile and υ_∞ which is terminal wind velocity. The β-law sets the wind acceleration at the sonic point as

$$a = \upsilon\frac{d\upsilon}{dr} = \left[\upsilon_s + (\upsilon_\infty - \upsilon_s)\Big(1 - \frac{r_s}{r}\Big)^\beta\right]\left[\frac{R\upsilon_\infty\beta}{r^2}\left(1 - \frac{r_s}{r}\right)^{\beta-1}\right]. \tag{E.2}$$

For a given value of sound speed υ_s and sonic point radius, the equation 2.7 allows to construct a relation between the wind acceleration at the sonic point, β and υ_∞. This relation is shown in figure E.1 (top panel). It shows that for a given β and υ_∞ there is a single value of acceleration at the sonic point. However, for a given value of wind acceleration at the sonic point a_s, there exist a range of possible β and υ_∞. The bottom panel of the Fig. E.1 shows the a_s from the stellar structure models. Importantly, the υ_s and R_s **are not constant** across this plot. Every model has its own υ_s and R_s, (for the latter it is seen from the figure 4.2) which does not allow to use a single diagram, such as the top panel of E.1, to display all Galactic WNE stars.

In order to analyze the wind parameters of the Galactic WNE stars we perform the following procedure. Appointing the β-law and fixing β allows to obtain the υ_∞ uniquely for a given a_s. We further limit the range of υ_∞ to $\upsilon_\infty \in (1400, 3000)$ which corresponds to the values found for the Galactic WNE stars (Hamann et al. 2006, Gräfener et al. 2017).

The constraint on υ_∞ implies that there is also a constraint on a_s for a given value of β. Otherwise, if the υ_∞ is not constrained, the single $\beta = 1.0$ would allow to obtain υ_∞ for all values of a_s,

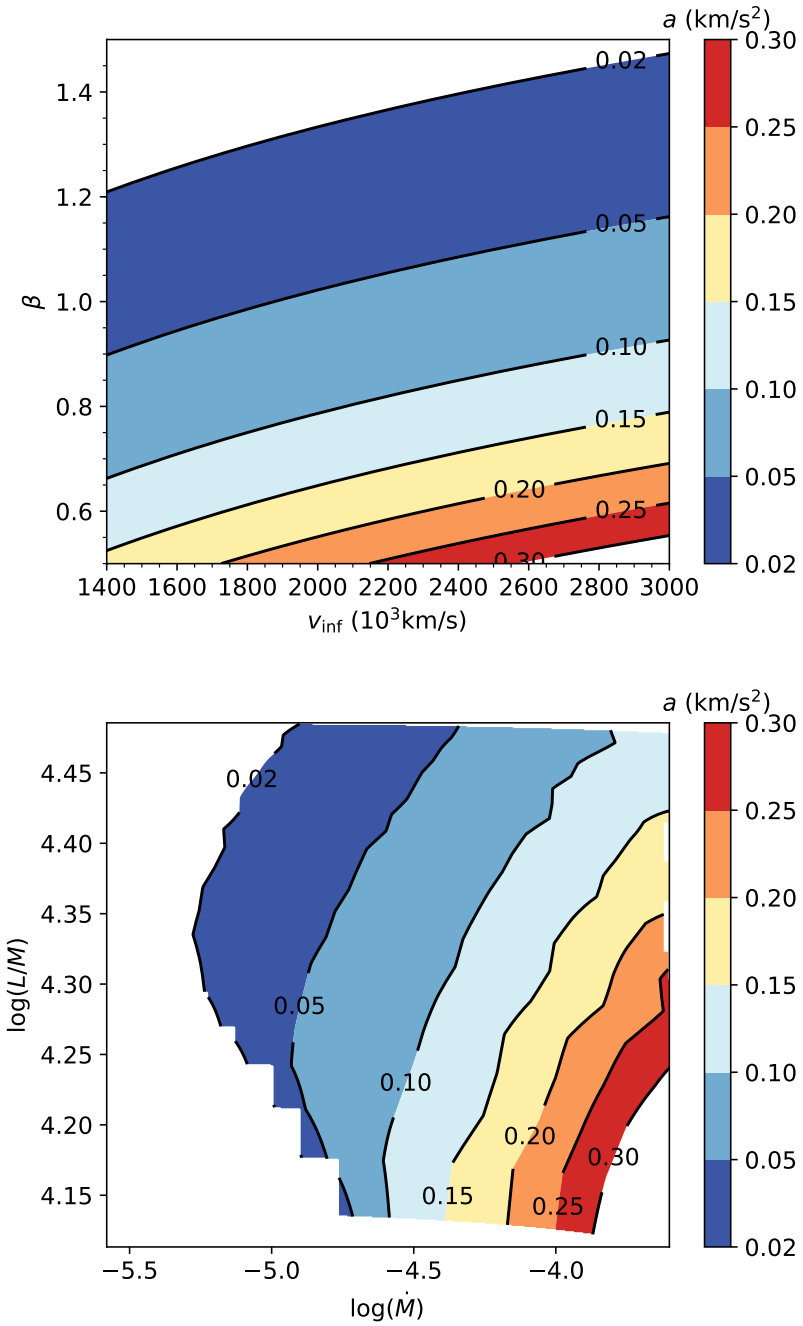

Figure E.1.: Top panel: The $\beta - v_{inf}$ map of the β-velocity law, computed for the commonly found $v_s = 40$ km/s and $R_s = 1R_\odot$ in the H-free helium models with Galactic metallicity. Bottom panel: Acceleration a (km/s^2) as a function of mass-loss rate and luminosity-to-mass ratio of the set of our models in the mass range $M \in (10 - 30)M_\odot$.

or equivalently, for all WNE stars. However, for those in the upper-left and bottom-right corners of the Fig. E.2, the values of the terminal velocity would be too low and too high, respectively (compare to observed ones).

This is shown in the figure E.2, where, for example, for a $\beta = 1.0$ only the a_s from models with approximately $\log(\dot{M}) \in (-4.75, -4.20)$ result in υ_∞ within aforementioned range. Thus we select

three values of $\beta = \{0.9, 1.0, 1.15\}$ that lead to full coverage of the parameter space of observed WNE stars.

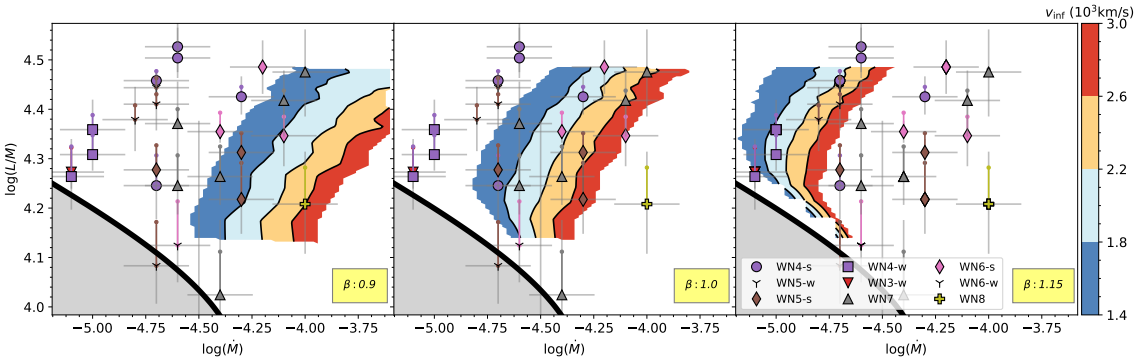

Figure E.2.: All three panels are $\dot{M} - L/M$ plots with color-coded v_{inf} for different values of β, shown in yellow boxes. WNE stars are plotted using the mass-loss rates from Hamann et al. (2006) and GAIA luminosities. (For the error bar description, see 4.4)

Interestingly, figure E.2, suggests that a single value of β, in particular, the most widely adopted $\beta = 1$ cannot explain neither most of the early-type WN4 nor the latest WN8. Most of WN4 stars with their relatively low mass-loss rates require lower value of β, or, equivalently, an overall steeper velocity gradient. In contrast, the late type WN8 requires higher, $\beta \approx 1.15$ to have terminal velocity in the observable range. However, we note that overall, the range of β for Galactic WNE stars is rather narrow.
For completeness, we analyze the effects of increased metallicity and chemical evolution on the wind acceleration at the sonic point.

E.0.1. Metallicity effect on the wind acceleration

Here we investigate, if a higher metallicity, $Z = 2Z_{\odot}$, affects the initial wind acceleration.
Increase in metallicity forces a star to inflate, meaning that R_s is higher for a higher metallicity model. In addition, a more prominent IOB leads to the sonic point being located at higher temperatures, and consequently, higher sound speed. However, the decrease in velocity profile steepness due to inflation counterbalances the rise in u_s, resulting in a a_s similar to the one from the model with Galactic metallicity.
The net effect is that, in the parameter range covered by our models ($M \in (10, 16)M_{\odot}$) for the supersolar metallicity, the wind acceleration at the sonic point is similar to the Galactic models. In other words, a given β law, with defined $(\upsilon_{\infty}, \beta)$ may account for both $Z = Z_{\odot}$ and $Z = 2Z_{\odot}$. Meanwhile there is a considerable difference in the T_s, which, if included into a temperature stratification model, may result in a different T_{eff} at the photosphere. In this case, 2 stars with the same L/M and $\dot{M}$ will have different T_{eff}, or equivalently, different subclasses.
More detailed investigation is required to confirm that proposal.

E.0.2. Evolutionary effects on the wind acceleration

Here we discuss, how the chemical evolution during core helium burning affects the sonic point conditions and the wind acceleration.
During the WNE phase there is a steady decrease in luminosity and in sonic radius (which occurs in response to the growing core of inert carbon). Due to the persistent loss of mass, however, the change in L/M is small. We note here, that previously we mentioned the evolutionary uncertainties

on the L/M of observed WNE stars. In that case we assumed a constant luminosity (an observed one) and based on that we obtained a range of possible L/M. In opposite here, we have a changing L as well as stellar mass. Alongside with the absence of any noticeable change in L/M, our models maintain an almost constant T_s, u_s and a_s during the WNE phase.
Thus, we conclude that the chemical evolution withing the WNE phase of the compact Galactic model does not result in any significant changes in sonic point conditions, except the overall decrease in the R_s and thus does not affect the photospheric conditions.

Appendix F.

Note on the wind models with LMC metallicity

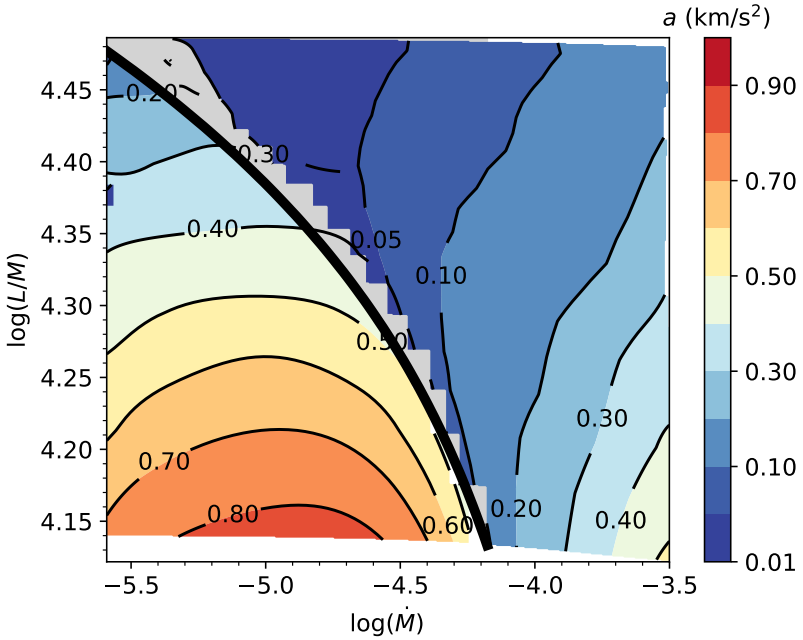

Figure F.1.: Acceleration a (km/s^2) as a function of mass-loss rate and luminosity-to-mass ratio of the set of our models in mass diapason $M \in (10-30)M_\odot$ with LMC metallicity. Black solid line is a critical $\dot{M} - L/M$ curve.

In this section we discuss wind models computed to reproduce the observed parameters of WNE stars in LMC, in particular the mass-loss rate, terminal velocity and the L/M using the same method as in section E.

In contrast to the Galactic case, here there are two regions with different sonic point conditions, including the initial wind acceleration. Figure F.2 shows that in the compact domain, above the critical curve, values and overall distribution of a_s is similar to the Galactic case (Fig. E.2). However, below the critical curve, the extended models exhibit a much higher wind acceleration at the sonic point. This can already be seen from the velocity profile of the $20M_\odot$ model (Fig. 5.1). From the corresponding table (Table. 5.2) it follows that such large acceleration is solely caused by the high velocity gradient at the sonic point, while the u_s is lower for the extended solutions. This can be understood from the steepness on the opacity profiles, which is much larger for the helium

II opacity bump than for IOB (Fig. 2.1, bottom panel), while the value of κ at the sonic point is similar between IOB and HOB solutions for massive stars (see Tbl. 5.1), which are inherently inflated.

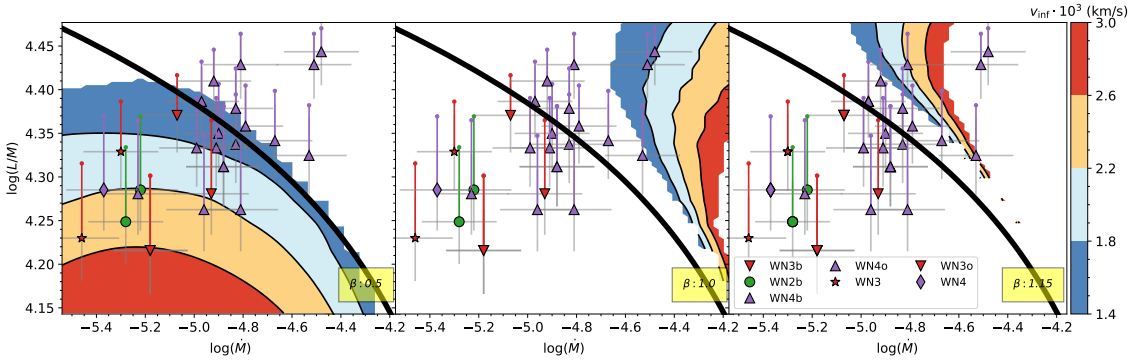

Figure F.2.: All three panels are $\dot{M} - L/M$ plots with color-coded v_∞ for different values of β, shown in yellow boxes. WNE stars are plotted using the mass-loss rates from Hainich et al. (2014). For the error bar description, see 4.4)

Large wind acceleration at the sonic point, as we previously pointed out requires a more steep β-law, which can be achieved either with setting large v_∞ or low β (see Fig. E.1 top panel). However, we are limited by the observed values of v_∞. As before, we assume a range $v_\infty \in (1400, 3200)$km/s and investigate what values of β are required to reproduced the observed WNE population.
The result of this analysis is displayed in the figure F.2. Second and third panel of that figure show that the compact part of the population, the luminous WN4, can be reproduced by the $\beta \approx 1.00$, similarly to the Galactic case E.2. However, the extended WN2, WN3 & WN4 require a much smaller $\beta \approx 0.5$. Such a steep velocity profile implies that the terminal velocity is reached much sooner in terms of radius. Notably, the commonly adopted $\beta = 1$ law would result in no physically relevant solutions in this region. This has previously been reported by Gräfener et al. (2017).
However, the results mentioned above strongly depend on the location of the critical curve, which, in turn, depends on the metallicity (see Fig. 5.2). In case of $Z = 0.004$, almost entire WN4 population can be reproduced by the $\beta \approx 1$ law with the same properties as the Galactic WNE stars (Fig. E.2). In contrast, if $Z = 0.01$ is adopted, the $\beta \approx 0.5$ would explain almost all WNE in LMC.
At the end, out models may prove to be usefull in a more detailed investigation of the wind structure of the LMC WNE stars, where the sonic point parameters and β can be used as ab inito for the computation of the temperature stratification and determination of the photospheric conditions.

Bibliography

Abbott, B. P., Abbott, R., Abbott, T. D., Abernathy, M. R., Acernese, F., Ackley, K., Adams, C., Adams, T., Addesso, P., Adhikari, R. X., and et al. (2016). Observation of Gravitational Waves from a Binary Black Hole Merger. *Physical Review Letters*, 116(6):061102.

Abbott, B. P., Abbott, R., Abbott, T. D., Acernese, F., Ackley, K., Adams, C., Adams, T., Addesso, P., Adhikari, R. X., Adya, V. B., and et al. (2017). GW170817: Observation of Gravitational Waves from a Binary Neutron Star Inspiral. *Physical Review Letters*, 119(16):161101.

Berrington, K. (1995). Summary of the Iron and Opacity Projects. In Adelman, S. J. and Wiese, W. L., editors, *Astrophysical Applications of Powerful New Databases*, volume 78 of *Astronomical Society of the Pacific Conference Series*, page 19.

Braginskii, S. I. (1965). Transport Processes in a Plasma. *Reviews of Plasma Physics*, 1:205.

Brown, W. R., Lattanzi, M. G., Kenyon, S. J., and Geller, M. J. (2018). Gaia and the Galactic Center Origin of Hypervelocity Stars. *ArXiv e-prints*.

Castelvecchi, D. (2018). Billion-star map of Milky Way set to transform astronomy. *NATURE*, 557:18–18.

Choudhury, S., Subramaniam, A., and Cole, A. A. (2016). Photometric metallicity map of the Large Magellanic Cloud. *MNRAS*, 455:1855–1880.

Crowther, P. A. (2007). Physical Properties of Wolf-Rayet Stars. *ARA&A*, 45:177–219.

Cui, X.-H., Liang, E.-W., Lv, H.-J., Zhang, B.-B., and Xu, R.-X. (2010). Towards the properties of long gamma-ray burst progenitors with Swift data. *MNRAS*, 401:1465–1474.

Draine, B. T. (2011). *Physics of the Interstellar and Intergalactic Medium*.

Drazdauskas, A., Tautvaišienė, G., Smiljanic, R., Bagdonas, V., and Chorniy, Y. (2016). Chemical composition of evolved stars in the young open clusters NGC 4609 and NGC 5316. *MNRAS*, 462:794–803.

Eddington, A. S. (1925). A limiting case in the theory of radiative equilibrium. *MNRAS*, 85:408.

Gräfener, G. and Hamann, W.-R. (2005). Hydrodynamic model atmospheres for WR stars. Self-consistent modeling of a WC star wind. *A&A*, 432:633–645.

Gräfener, G., Owocki, S. P., Grassitelli, L., and Langer, N. (2017). On the optically thick winds of Wolf-Rayet stars. *A&A*, 608:A34.

Gräfener, G., Owocki, S. P., and Vink, J. S. (2012a). Stellar envelope inflation near the Eddington limit. Implications for the radii of Wolf-Rayet stars and luminous blue variables. *A&A*, 538:A40.

Gräfener, G., Vink, J. S., and Owocki, S. P. (2012b). Massive Stars Near the Eddington Limit: Mass Loss and Envelope Inflation. In Drissen, L., Robert, C., St-Louis, N., and Moffat, A. F. J., editors, *Proceedings of a Scientific Meeting in Honor of Anthony F. J. Moffat*, volume 465 of *Astronomical Society of the Pacific Conference Series*, page 202.

Grassitelli, L. (2016). *Instabilities in the envelope of stars*. PhD thesis, Argelander Institute for Astronomy, University of Bonn, Germany.

Grassitelli, L., Chené, A.-N., Sanyal, D., Langer, N., St-Louis, N., Bestenlehner, J. M., and Fossati, L. (2016a). Diagnostics of the unstable envelopes of Wolf-Rayet stars. *A&A*, 590:A12.

Grassitelli, L., Fossati, L., Langer, N., Simón-Díaz, S., Castro, N., and Sanyal, D. (2016b). Metallicity dependence of turbulent pressure and macroturbulence in stellar envelopes. *A&A*, 593:A14.

Grassitelli, L., Langer, N., Grin, N. J., Mackey, J., Bestenlehner, J. M., and Graefener, G. (2018). Subsonic structure and optically thick winds from Wolf–Rayet stars. *ArXiv e-prints*.

Gray, D. F. (2005). *The Observation and Analysis of Stellar Photospheres*.

Hainich, R., Rühling, U., Pasemann, D., and Hamann, W.-R. (2015). The WN population in the Magellanic Clouds. In Hamann, W.-R., Sander, A., and Todt, H., editors, *Wolf-Rayet Stars: Proceedings of an International Workshop held in Potsdam, Germany, 1-5 June 2015. Edited by Wolf-Rainer Hamann, Andreas Sander, Helge Todt. Universitätsverlag Potsdam, 2015., p.117-120*, pages 117–120.

Hainich, R., Rühling, U., Todt, H., Oskinova, L. M., Liermann, A., Gräfener, G., Foellmi, C., Schnurr, O., and Hamann, W.-R. (2014). The Wolf-Rayet stars in the Large Magellanic Cloud. A comprehensive analysis of the WN class. *A&A*, 565:A27.

Hamann, W.-R., Gräfener, G., and Liermann, A. (2006). The Galactic WN stars. Spectral analyses with line-blanketed model atmospheres versus stellar evolution models with and without rotation. *A&A*, 457:1015–1031.

Haschke, R., Grebel, E. K., Duffau, S., and Jin, S. (2012). Metallicity Distribution Functions of the Old Populations of the Magellanic Clouds from RR Lyrae Stars. *AJ*, 143:48.

Heger, A. (2013). Astrophysics: Going supernova. *Nature*, 494:46–47.

Iglesias, C. A. and Rogers, F. J. (1996). Updated Opal Opacities. *ApJ*, 464:943.

Joss, P. C., Salpeter, E. E., and Ostriker, J. P. (1973). On the "Critical Luminosity" in Stellar Interiors and Stellar Surface Boundary Conditions. *ApJ*, 181:429–438.

Kippenhahn, R. and Weigert, A. (1990). *Stellar Structure and Evolution*.

Kippenhahn, R. and Weigert, A. (1994). *Stellar Structure and Evolution*.

Lamers, H. J. G. L. M. (2004). Mass Loss and Stellar Rotation (Invited Review). In Maeder, A. and Eenens, P., editors, *Stellar Rotation*, volume 215 of *IAU Symposium*, page 479.

Lamers, H. J. G. L. M. and Cassinelli, J. P. (1999). *Introduction to Stellar Winds*.

Langer, N. (1989). Standard models of Wolf-Rayet stars. *A&A*, 210:93–113.

Langer, N. (1997). The Eddington Limit in Rotating Massive Stars. In Nota, A. and Lamers, H., editors, *Luminous Blue Variables: Massive Stars in Transition*, volume 120 of *Astronomical Society of the Pacific Conference Series*, page 83.

Langer, N. (2012). Presupernova Evolution of Massive Single and Binary Stars. *ARA&A*, 50:107–164.

Langer, N., Kiriakidis, M., El Eid, M. F., Fricke, K. J., and Weiss, A. (1988). The surface temperature of C/O-rich Wolf-Rayet stars. *A&A*, 192:177–181.

Lighthill, M. J. (1952). On Sound Generated Aerodynamically. I. General Theory. *Proceedings of the Royal Society of London Series A*, 211:564–587.

Lu, L., Sargent, W. W. L., and Barlow, T. A. (1998). Elemental Abundances in Quasar Absorption Line Systems. *Highlights of Astronomy*, 11:90.

Lundstrom, I. and Stenholm, B. (1984). Wolf-Rayet stars in open clusters and associations. *A&AS*, 58:163–192.

Marchenko, S. V. and Moffat, A. F. J. (1998). Time-Frequency Analysis of Three Strongly Variable Wolf-Rayet Stars: WR 6, WR 134, and WR 123. *ApJ*, 499:L195–L198.

McWilliam, A. (2016). The Chemical Composition of the Galactic Bulge and Implications for its Evolution. *PASA*, 33:e040.

Meynet, G. and Maeder, A. (2003). Stellar evolution with rotation. X. Wolf-Rayet star populations at solar metallicity. *A&A*, 404:975–990.

Mihalas, D. (1978). *Stellar atmospheres /2nd edition/*.

Moffat, A. F. J., Drissen, L., Lamontagne, R., and Robert, C. (1988). Spectroscopic evidence for rapid blob ejection in Wolf-Rayet stars. *ApJ*, 334:1038–1043.

Nakauchi, D. and Saio, H. (2018). Helium Star Models with Optically Thick Winds: Implications for the Internal Structures and Mass-loss Rates of Wolf-Rayet Stars. *ApJ*, 852:126.

Nazé, Y., Rauw, G., Manfroid, J., Chu, Y.-H., and Vreux, J.-M. (2003). WR bubbles and He II emission. *A&A*, 408:171–186.

Ness, M. and Freeman, K. (2016). The Metallicity Distribution of the Milky Way Bulge. *PASA*, 33:e022.

Nugis, T. and Lamers, H. J. G. L. M. (2002a). The mass-loss rates of Wolf-Rayet stars explained by optically thick radiation driven wind models. *A&A*, 389:162–179.

Nugis, T. and Lamers, H. J. G. L. M. (2002b). The mass-loss rates of Wolf-Rayet stars explained by optically thick radiation driven wind models. *A&A*, 389:162–179.

Oskinova, L. M., Hamann, W.-R., and Feldmeier, A. (2007). Neglecting the porosity of hot-star winds can lead to underestimating mass-loss rates. *A&A*, 476:1331–1340.

Pedicelli, S., Bono, G., Lemasle, B., François, P., Groenewegen, M., Lub, J., Pel, J. W., Laney, D., Piersimoni, A., Romaniello, M., Buonanno, R., Caputo, F., Cassisi, S., Castelli, F., Leurini, S., Pietrinferni, A., Primas, F., and Pritchard, J. (2009). On the metallicity gradient of the Galactic disk. *A&A*, 504:81–86.

Petrovic, J., Pols, O., and Langer, N. (2006). Are luminous and metal-rich Wolf-Rayet stars inflated? *A&A*, 450:219–225.

Rybicki, G. B. and Lightman, A. P. (1979). *Radiative processes in astrophysics*.

Salpeter, E. E. (1955). The Luminosity Function and Stellar Evolution. *ApJ*, 121:161.

Sander, A., Hamann, W.-R., Hainich, R., Shenar, T., and Todt, H. (2015). Hydrodynamic modeling of massive star atmospheres. In Hamann, W.-R., Sander, A., and Todt, H., editors, *Wolf-Rayet Stars: Proceedings of an International Workshop held in Potsdam, Germany, 1-5 June 2015. Edited by Wolf-Rainer Hamann, Andreas Sander, Helge Todt. Universitätsverlag Potsdam, 2015., p.139-142*, pages 139–142.

Sander, A., Hamann, W.-R., and Todt, H. (2012). The Galactic WC stars. Stellar parameters from spectral analyses indicate a new evolutionary sequence. *A&A*, 540:A144.

Sander, A. A. C., Hamann, W.-R., Todt, H., Hainich, R., Shenar, T., Ramachandran, V., and Oskinova, L. M. (2018). The Galactic WC and WO stars: The impact of revised distances from Gaia DR2 and their role as massive black hole progenitors. *ArXiv e-prints*.

Sanyal, D., Grassitelli, L., Langer, N., and Bestenlehner, J. M. (2015). Massive main-sequence stars evolving at the Eddington limit. *A&A*, 580:A20.

Sanyal, D., Langer, N., Szécsi, D., -C Yoon, S., and Grassitelli, L. (2017). Metallicity dependence of envelope inflation in massive stars. *A&A*, 597:A71.

Schaerer, D., Contini, T., and Pindao, M. (1999). New catalogue of Wolf-Rayet galaxies and high-excitation extra-galactic HII regions. *A&AS*, 136:35–52.

Taam, R. E. and Sandquist, E. L. (2000). Common Envelope Evolution of Massive Binary Stars. *ARA&A*, 38:113–141.

Turck-Chièze, S., Le Pennec, M., Ducret, J. E., Colgan, J., Kilcrease, D. P., Fontes, C. J., Magee, N., Gilleron, F., and Pain, J. C. (2016). Detailed Opacity Comparison for an Improved Stellar Modeling of the Envelopes of Massive Stars. *ApJ*, 823:78.

Vink, J. S. and de Koter, A. (2005). On the metallicity dependence of Wolf-Rayet winds. *A&A*, 442:587–596.

Yoon, S.-C. (2017). Towards a better understanding of the evolution of Wolf-Rayet stars and Type Ib/Ic supernova progenitors. *MNRAS*, 470:3970–3980.

Yoon, S.-C. and Langer, N. (2005). Evolution of rapidly rotating metal-poor massive stars towards gamma-ray bursts. *A&A*, 443:643–648.

List of Figures

List of Tables